Accurate numerical simulations of inspiralling binary neutron stars and their comparison with effective-one-body analytical models

Luca Baiotti, Thibault Damour, Bruno Giacomazzo, Alessandro Nagar, and Luciano Rezzolla

Phys. Rev. D **84**, 024017 — Published 12 July 2011

DOI: 10.1103/PhysRevD.84.024017

Accurate numerical simulations of inspiralling binary neutron stars and their comparison with effective-one-body analytical models

Luca Baiotti,[1] Thibault Damour,[2,3] Bruno Giacomazzo,[4,5] Alessandro Nagar,[2] and Luciano Rezzolla[6,7]

[1] *Institute of Laser Engineering, Osaka University, Suita, Japan*
[2] *Institut des Hautes Etudes Scientifiques, Bures-sur-Yvette, France*
[3] *ICRANet, Pescara, Italy*
[4] *Department of Astronomy, University of Maryland, College Park, MD USA*
[5] *Gravitational Astrophysics Laboratory, NASA Goddard Space Flight Center, Greenbelt, MD USA*
[6] *Max-Planck-Institut für Gravitationsphysik, Albert-Einstein-Institut, Potsdam, Germany*
[7] *Department of Physics and Astronomy, Louisiana State University,Baton Rouge, LA, USA*

Binary neutron-star systems represent one of the most promising sources of gravitational waves. In order to be able to extract important information, notably about the equation of state of matter at nuclear density, it is necessary to have in hands an accurate analytical model of the expected waveforms. Following our recent work [1], we here analyze more in detail two general-relativistic simulations spanning about 20 gravitational-wave cycles of the inspiral of equal-mass binary neutron stars with different compactnesses, and compare them with a tidal extension of the effective-one-body (EOB) analytical model. The latter tidally extended EOB model is analytically complete up to the 1.5 post-Newtonian level, and contains an analytically undetermined parameter representing a higher-order amplification of tidal effects. We find that, by calibrating this single parameter, the EOB model can reproduce, within the numerical error, the two numerical waveforms essentially up to the merger. By contrast, analytical models (either EOB or Taylor-T4) that do not incorporate such a higher-order amplification of tidal effects, build a dephasing with respect to the numerical waveforms of several radians.

PACS numbers: 04.25.dk, 04.25.Nx, 04.30.Db, 04.40.Dg, 95.30.Sf, 97.60.Jd

I. INTRODUCTION

Binary neutron-star inspirals are among the most promising and certain target sources for the advanced versions of the currently operating ground-based gravitational-wave (GW) detectors LIGO/Virgo/GEO. These detectors will be maximally sensitive during the inspiral part of the signal (around a GW frequency of 100 Hz, i.e., significantly below the typical GW frequencies at merger, which are around 1000 Hz). The inspiral part of the signal will be influenced by tidal interaction between the two neutron stars (NSs), which, in turn, encodes important information about the equation of state (EOS) of matter at nuclear densities. In other words, the detection of GWs emitted from inspiralling NS in the LIGO/Virgo bandwidth could enable us to acquire important information about the EOS of NS matter. However, besides getting sufficiently accurate GW data from advanced detectors, two conditions must be fulfilled for the success of this program: (i) obtaining a large enough sample of accurate numerical simulations of inspiralling binary neutron stars (BNS); (ii) possessing a sufficiently accurate *analytical model* of inspiralling BNS, allowing the extrapolation of the finite set of numerical simulations to the multi-parameter space of possible GW templates. Extending the work recently reported in [1], we here address issues and provide useful progress on both of them. In essence, we will present the results of general-relativistic simulations spanning about 20 gravitational-wave cycles of the inspiral of equal-mass BNSs, and show how a suitably calibrated effective-one-body (EOB) analytical model of tidally interacting BNS systems enables us to accurately reproduce the numerically simulated inspiral waveform.

Numerical simulations of merging BNSs in full general relativity have a long history (see the Introduction of [2] for a brief review), and the first merger to a hypermassive neutron star (HMNS) was computed more than ten years ago [3]. However, it is only in recent years and with the use of more advanced and accurate numerical algorithms that it has been possible to obtain a more precise and robust description of this process and to include additional physical ingredients such as magnetic fields and realistic EOSs. In particular the use of adaptive mesh refinement techniques [2, 4, 5] made it possible to use very high resolutions, increasing not only the level of accuracy, but giving the possibility, for example, to compute the full evolution of the HMNS up to black-hole (BH) formation [2] or to investigate in detail the development of hydrodynamical instabilities at the time of the merger [2]. Also the numerical convergence properties of BNS simulations have been studied only recently [6], providing for the first time evidence of the level of accuracy that it is now possible to achieve in the generation of GW templates from these sources. Several groups are now able to simulate BNSs using more realistic EOSs (see, e.g., [7–9] and references therein) and to assess the possibility to measure their effects in the GW signals. In the last two years three different groups were also able to perform for the first time the simulations of magnetized BNSs [10–12]. One conclusion already reached is that no effect of the magnetic field can be measured in the inspi-

ral waveforms [12], while the role of the magnetic field in the post-merger phase has been recently investigated in [13] as well as its role in the emission of relativistic jets after the collapse to BH [14]. Because of their possible connection with the production of short gamma-ray bursts (GRBs), numerical simulations have also investigated in detail the formation of massive tori and their dependence on the initial mass and mass ratio of the binary (see e.g., [15]) as well as on the EOS used (see [8, 9] and references therein).

On the other hand, the program of developing an analytical description within general relativity of tidally-interacting binary systems has been initiated only recently [16–22]. Overall, this work has brought to light two surprising results. First, that the dimensionless expression k_ℓ (Love number) in the (gravito-electric) tidal polarizability parameter $G\mu_\ell \equiv 2k_\ell R^{2\ell+1}/(2\ell-1)!!$ measuring the relativistic coupling (of multipolar order ℓ) between a NS of radius R and the external gravitational field in which it is embedded strongly decreases with the compactness parameter $\mathcal{C} \equiv GM/(c^2R)$ of the NS [18, 19][1]. Second, a recent comparison between a numerical computation of the binding energy of quasi-equilibrium circular sequences of BNS systems [23] and the EOB description of tidal effects [21] suggests that high-order (beyond the first order) post-Newtonian (PN) corrections to tidal effects tend to significantly increase (typically by a factor of order two) the effective tidal polarizability of NSs.

The main aim of this paper is to present a detailed comparison between waveforms computed from the tidal-completed EOB analytical model of Ref. [21] and waveforms from BNS simulations comprising between $\simeq 20$ and 22 GW cycles of inspiral [1]. More specifically, we will follow Ref. [21], which has proposed a new way of analytically describing the dynamics of tidally interacting BNSs, whose validity is not a priori limited (like the purely PN-based descriptions used in, e.g., [16]) to the low-frequency part of the GW signal, but may be extended to higher frequencies, essentially up to the merger. The proposal of Ref. [21] consists in extending the EOB method [24–26], which has recently shown its ability to accurately describe the GW waveforms emitted by inspiralling, merging, and ringing binary black holes (BBHs) [27, 28], by incorporating tidal effects in it. We will improve the tidally-extended EOB model of Ref. [21] (which already contained the 1PN contributions to the dynamics) by incorporating the 1PN contributions to the waveform (from [29]), as well as the waveform tail effects (from [30, 31]).

The paper is organized as follows. In Sec. II we present in detail our numerical simulations, briefly reviewing our numerical setup, discussing the dynamics of the binaries, and presenting the main features of the waveforms. Section III deals instead with the analytical models of the binary dynamics and of waveforms that include tidal interaction (either PN-based or EOB-based). Sec. IV introduces some tools, notably a certain intrinsic representation of the time evolution of the GW frequency, which is useful for doing the numerical-relativity/analytical-relativity (NR/AR) comparison. Section V discusses the various errors that affect the NR phasing. The NR/AR comparison is carried out in Sec. VI. We finally present a summary of our findings in Sec. VII. Two appendices give additional technical details on the use of the waveforms from the numerical-relativity simulations.

We use a spacelike signature $(-,+,+,+)$ and (unless explicitly said otherwise) a system of units in which $c = G = M_\odot = 1$. Greek indices are taken to run from 0 to 3, Latin indices from 1 to 3.

II. NUMERICAL-RELATIVITY SIMULATIONS

A. Numerical setup

The numerical simulations were performed with the set of codes `Cactus-Carpet-Whisky` [32–36]. The reader is referred to these references for the description of the details of the implementations and of the tests of the codes. Since in this work we use the same gauges and numerical methods already applied and explained in [2, 6], we also refer the reader to these articles for more detailed explanations of the setup only briefly recalled below.

In essence, we evolve a conformal-traceless "3+1" formulation of the Einstein equations in which the spacetime is decomposed into three-dimensional spacelike slices, described by a metric γ_{ij}, its embedding in the full spacetime, specified by the extrinsic curvature K_{ij}, and the gauge functions α (lapse) and β^i (shift), which specify a coordinate frame (see Ref. [34] for details on the latest implementation of the Einstein equations in the code). For the evolution of the matter, the `Whisky` code implements the flux-conservative formulation of the general-relativistic hydrodynamics equations proposed by the Valencia group [37]. Among its important features is that the set of conservation equations for the stress-energy tensor $T^{\mu\nu}$ and for the matter current density J^μ are written in hyperbolic, first-order, and flux-conservative form (see Ref. [2] for details on the latest implementation of the hydrodynamics equations in the code).

As initial data we use quasi-equilibrium binaries generated with the multi-domain spectral-method code `LORENE` developed at the Observatoire de Paris-Meudon [38]. For more information on the code and its methods, the reader is referred to the `LORENE` web pages [39]. In particular, we use irrotational configurations, defined as having vanishing vorticity and obtained under the additional assumption of a conformally flat spacetime metric [38]. The EOS assumed for the initial data is in

[1] As a consequence, for a given EOS, the Love numbers of a typical ($\mathcal{C} \simeq 0.15$) NS are found to be about 4 time smaller than their corresponding Newtonian estimates, that assume $\mathcal{C} \to 0$.

TABLE I. Properties of the binary NS initial data. From left to right the columns show: the name of the model, the total baryonic mass $M_{\rm tot}^{\rm bar}$ of the system, the total (initial) Arnowitt-Deser-Misner (ADM) mass $M_{\rm ADM}$ of the system, the total (initial) angular momentum J, the initial orbital frequency $f_{\rm orb}$, the initial maximum rest-mass density $\rho_{\rm max}$, the mean radius $\bar{r}$ of each star, the axis ratio $\bar{A}$ of each star, the individual ADM mass M^∞ of each star as considered in isolation at infinity, the compactness $\mathcal{C}^\infty = M^\infty_{NS}/R^\infty_{NS}$ of each star as considered in isolation at infinity, the corresponding (quadrupolar) dimensionless Love number k_2 and tidal constant κ_2^T as defined in Ref. [21] (see also Eq. (13) below). The mean radius is defined as $\bar{r} \equiv (r_{\vdash} + r_{\dashv} + r_{\perp} + r_{\rm pol})/4$, where $r_{\vdash}$ and $r_{\dashv}$ are the (coordinate) radii of the star parallel to the line connecting the stars, $r_{\perp}$ is the radius in the equatorial plane perpendicular to that line, and $r_{\rm pol}$ is the radius perpendicular to the equatorial plane. The axis ratio is defined as the ratio between the mean radius parallel to the line connecting the stars and the mean radius in the plane perpendicular to that line, namely $\bar{A} \equiv (r_{\perp} + r_{\rm pol})/(r_{\vdash} + r_{\dashv})$. The values of $f_{\rm orb}$, $\bar{r}$, $\bar{A}$, M^∞, and $\mathcal{C}^\infty$ are computed with the `LORENE` code, the values of $M_{\rm tot}^{\rm bar}$, $M_{\rm ADM}$, J, and $\rho_{\rm max}$ are instead measured on the Cartesian grid by the `Whisky` code, and those of k_2 (and κ_2^T) are computed according to Ref. [18].

Model	$M_{\rm tot}^{\rm bar}$ ($M_\odot$)	$M_{\rm ADM}$ ($M_\odot$)	$J/10^{49}$ (g cm^2/s)	$f_{\rm orb}$ (Hz)	$\rho_{\rm max}/10^{14}$ (g/cm^3)	$\bar{r}$ (km)	$\bar{A}$	M^∞ ($M_\odot$)	$\mathcal{C}^\infty$	k_2	κ_2^T
`M2.9C.12`	2.8899	2.6925	7.1747	188.52	4.60	14.2	0.97	1.359	0.1196	0.09719	496.09
`M3.2C.14`	3.2504	2.9966	8.5558	197.03	5.93	13.2	0.97	1.514	0.1399	0.07894	183.81

all cases the polytropic EOS

$$p = K\,\rho^{\Gamma}\,, \tag{1}$$

where p and ρ are the pressure and the rest-mass (baryonic-mass) density, respectively. The chosen adiabatic index is $\Gamma = 2$, while the polytropic constant is $K \simeq 123.6$ (in units where $c = G = M_\odot = 1$). For this particular EOS, the allowed maximum baryonic mass for an individual stable NS is $2.00\,M_\odot$, thus leading to a maximum compactness $M_{\rm ADM}/R \simeq 0.25$. The initial coordinate separation of the stellar centers in all cases is $d = 60$ km.

The physical properties of the two binaries considered here are summarized in Table I, where we have adopted the following naming convention: `M%C#`, with `%` being replaced by the rounded total baryonic mass $M_{\rm tot}^{\rm bar}$ of the binary NS system and `#` by the compactness. As an example, `M2.9C.12` is the binary with total baryonic mass $M_{\rm tot}^{\rm bar} = 2.8899\,M_\odot$ and compactness $\mathcal{C} = 0.1196$. We note that at least as far as the tidal effects are concerned, the most important difference in the two sets of initial data is represented by the compactness, which is smaller in the binary `M2.9C.12` than in the binary `M3.2C.14`. Note that the dimensionless EOB parameter κ_2^T measuring the strength of the (conservative) quadrupolar interaction is nearly three times larger for $\mathcal{C} = 0.12$, than for $\mathcal{C} = 0.14$.

The initial data is then evolved either using the (isentropic) polytropic EOS (1) or using the (non-isentropic) "ideal-fluid" EOS defined by the condition

$$p = \rho\,\epsilon(\Gamma - 1), \tag{2}$$

where ϵ is the specific internal energy and $e = \rho(1+\epsilon)$ is the total energy density. Although these EOSs are idealized, they provide a reasonable approximation of the dynamics of NSs during the inspiral, so that we expect that the use of realistic EOSs (with similar compactnesses) would not change the main qualitative conclusions of this work. A detailed discussion of the consequences of using either EOS will be presented in Sec. V.

As mentioned above, the use of adaptive mesh-refinement techniques allows us to reach a considerable level of precision and for this we use the `Carpet` code [33] that implements a vertex-centered adaptive-mesh-refinement scheme adopting nested grids with a $2:1$ refinement factor for successive grid levels. We center the highest resolution level around the peak in the rest-mass density of each star. This represents our rather basic form of adaptive-mesh refinement. The timestep on each grid is set by the Courant condition (expressed in terms of the speed of light) and so by the spatial grid resolution for that level; the typical Courant coefficient is set to be 0.35. The time evolution is carried out using fourth-order accurate Runge-Kutta integration steps. Boundary data for finer grids are calculated with spatial prolongation operators employing fifth-order polynomials and with prolongation in time employing second-order polynomials.

In the results presented below we have used 6 levels of mesh refinement with the finest grid resolution of $\Delta_{\rm min} = 0.12\,M_\odot = 0.177\,$km and the coarsest (or wave-zone) grid resolution of $\Delta_{\rm max} = 3.84\,M_\odot = 5.67\,$km. Each star is completely covered by the finest grid, so that the high-density regions of the stars are tracked with the highest resolution available. The refined grids are then moved by tracking the position of the maximum of the rest-mass density as the stars orbit, and are finally merged when they overlap. In addition, a set of refined but fixed grids is set up at the center of the computational domain so as to capture the details of the Kelvin-Helmholtz instability (cf. [2]). The finest of these grids extends to $r = 7.5\,M_\odot = 11\,$km $= 5.52M$ for model `M2.9C.12` and $= 4.95M$ for model `M3.2C.14` (here and

in the following M denotes the gravitational mass of the system at infinite separation, namely the sum of the gravitational masses of each NS as computed individually in isolation, i.e., $M \equiv 2M_{NS}^{\infty}$ in the notation of Table I). A single grid-resolution covers then the region between $r = 150\,M_\odot = 221.5\,\mathrm{km}$ and $r = 514.56\,M_\odot = 755.24\,\mathrm{km}$ (or $r = 378.63M$ for `M2.9C.12` and $r = 339.87M$ for `M3.2C.14`), in which our wave extraction is carried out. The resolution is here $\Delta = 3.84\,M_\odot = 5.67\,\mathrm{km}$ and thus more than sufficient to accurately resolve the gravitational waveforms that have initially a wavelength of about 720 km.

A reflection symmetry condition across the $z = 0$ plane and a π-symmetry condition[2] across the $x = 0$ plane are used. A number of tests have been performed to ensure that both the hierarchy of the refinement levels described above and the resolutions used yield results that are numerically consistent although not always in a convergent regime at the time of merger (see the detailed discussion in Ref. [6]).

B. Overall matter dynamics and gravitational waveforms

We next briefly recall the physical properties of BNS inspiral and merger as discussed in Refs. [2, 6]. The inspiral proceeds at higher and higher frequencies until the time of the merger, just before which the stars decompress because of the tidal force. At the time of the merger, a Kelvin-Helmholtz instability develops in the shearing layer formed by the colliding stars, which could lead to an exponential growth of magnetic fields if these are present [40, 41]; such a large growth was not found in recent related works [12, 13], and no magnetic fields are included in the simulations reported here. If the total mass of the system is sufficiently large, the merged object immediately collapses to a Kerr BH, while, for smaller masses the merger remnant is a HMNS in a metastable equilibrium. Because of the excess angular momentum, the HMNS is also subject to a bar deformation, being responsible for a copious emission of gravitational radiation with peak amplitudes that are comparable or even larger than those at the merger (cf. Ref. [2]). As the bar-deformed HMNS loses energy and angular momentum via GWs, it contracts and spins up, thus further increasing the losses. The process terminates when the threshold to the collapse to BH is crossed and the HMNS then rapidly produces a rotating BH surrounded by a torus of hot and high-density material. Although this post-merger evolution of the binary is of great interest and is likely to yield a wealth of physical information, it will not be further considered in the present work, which is instead focussed on the analytical modelling of the inspiral phase, up to the merger.

The GW signal is extracted at different surfaces of constant coordinate radius $r_{\rm obs}$ by means of two distinct methods. The first one is based on the measurements of the non-spherical gauge-invariant perturbations of a Schwarzschild BH [42, 43]. The second and independent one uses instead the Newman-Penrose formalism so that the GW (metric) polarization amplitudes h_+ and $h_\times$ are then related to ψ_4 by (see Sec. IV of Ref. [2] for details of the Newman-Penrose scalar extraction in our setup)

$$\ddot{h}_+ - \mathrm{i}\ddot{h}_\times = \psi_4 = \sum_{\ell=2}^{\infty}\sum_{m=-\ell}^{\ell} \psi_4^{\ell m}\, {}_{-2}Y_{\ell m}(\theta,\phi), \qquad (3)$$

where we have introduced the (multipolar) expansion of ψ_4 in spin-weighted spherical harmonics [44] of spin-weight $s = -2$. The coordinate extraction radius is $r_{\rm obs} = 500\,M_\odot$ for both models, which corresponds to $r_{\rm obs}/M = 184.3$ for `M2.9C.12` and to $r_{\rm obs}/M = 165.1$ for `M3.2C.14`. The top panels of Fig. 1 summarizes most of the information related to the $\ell = m = 2$ curvature waveforms ψ_4^{22} for the `M2.9C.12` model (left panels) and for the `M3.2C.14` model (right panels). The top panels of the figures show together the modulus and the real part of the waveform; the bottom ones, illustrate the behavior of the instantaneous GW (curvature) frequency $M\omega_{22}$. Note that the inspiral waveform of `M2.9C.12` contains about 22 GW cycles, while that of `M3.2C.14` contains about 20 GW cycles. To fix conventions, let us recall that we write the waveform as a complex number according to

$$\psi_4^{\ell m} = |\psi_4^{\ell m}| e^{-\mathrm{i}\phi_{\ell m}}\,, \qquad (4)$$

so that the instantaneous (curvature) GW frequency is simply defined as $\omega_{\ell m} \equiv \dot{\phi}_{\ell m}$. After the initial junk radiation (cf. Ref. [45]) that is responsible for a spike in the modulus around $t = 200M$ together with incoherent oscillations in the frequency, the complex ψ_4^{22} waveform becomes circularly polarized (as expected for circularized inspiral), with a modulus that grows monotonically in time up to the merger (see upper panels of Fig. 1).

The matter dynamics is reflected in the behavior of the frequency: for both models we clearly see that ω_{22} grows monotonically during the inspiral phase, until it reaches a maximum around the "merger". In this work, we phenomenologically define the "NR merger" as the instant when the modulus of the metric waveform h_{22} (see below) reaches its (first) maximum. Roughly speaking, in our simulations the "dynamical range" of the dimensionless GW frequency parameter $M\omega_{22}$ during the inspiral (i.e., before the merger) is $0.015 \lesssim M\omega_{22} \lesssim 0.15$. Note that, if we were considering a conventional $1.4\,M_\odot - 1.4\,M_\odot$ BNS system, we would then have the correspondence $f_{\rm GW}/100\mathrm{Hz} \simeq 115.4 M\omega_{22}$ so that $M\omega_{22} = 0.015$ corresponds to $f_{\rm GW} \approx 173.1$ Hz, while $M\omega_{22} = 0.15$ corresponds to $f_{\rm GW} \approx 1731$ Hz.

[2] Stated differently, we evolve only the region $\{x \geq 0, z \geq 0\}$ applying a 180-degree rotational-symmetry boundary condition across the plane at $x = 0$.

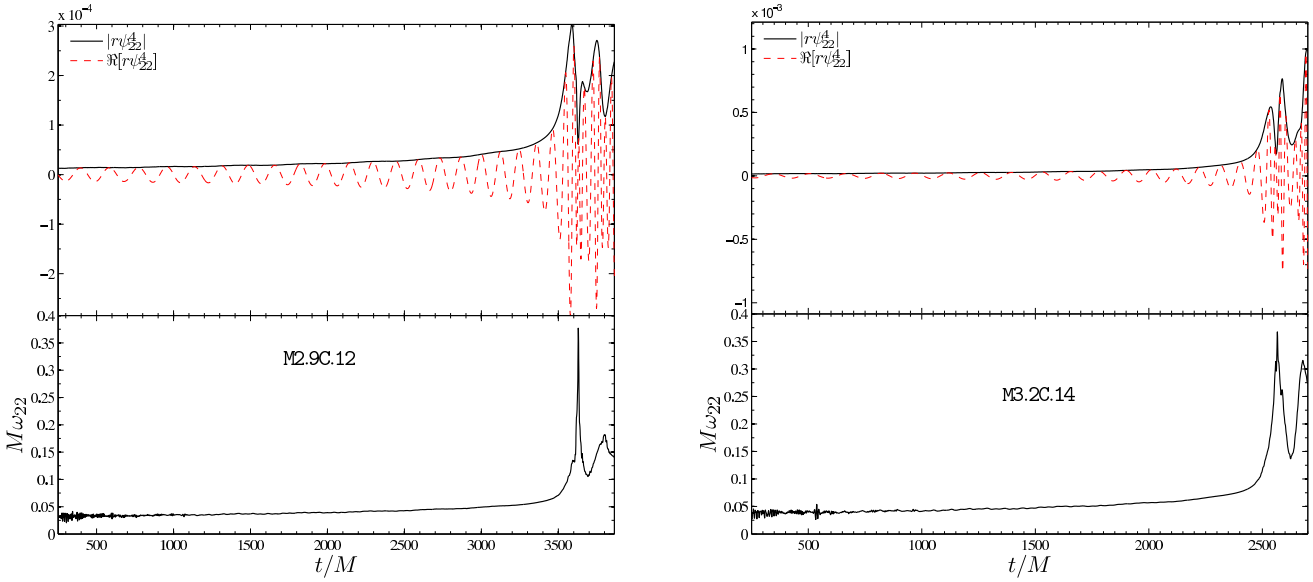

FIG. 1. Curvature gravitational waveforms $r\psi_4^{22}$ (upper panels) and their instantaneous frequency $M\omega_{22}$ (lower panels) for the `M2.9C.12` (left) and `M3.2C.14` (right) models. In both cases, the observer's (coordinate) extraction radius is $r_{\rm obs} = 500\,M_\odot$; this corresponds to $r_{\rm obs}/M = 184.3$ for `M2.9C.12` and $r_{\rm obs}/M = 165.1$ for `M3.2C.14`.

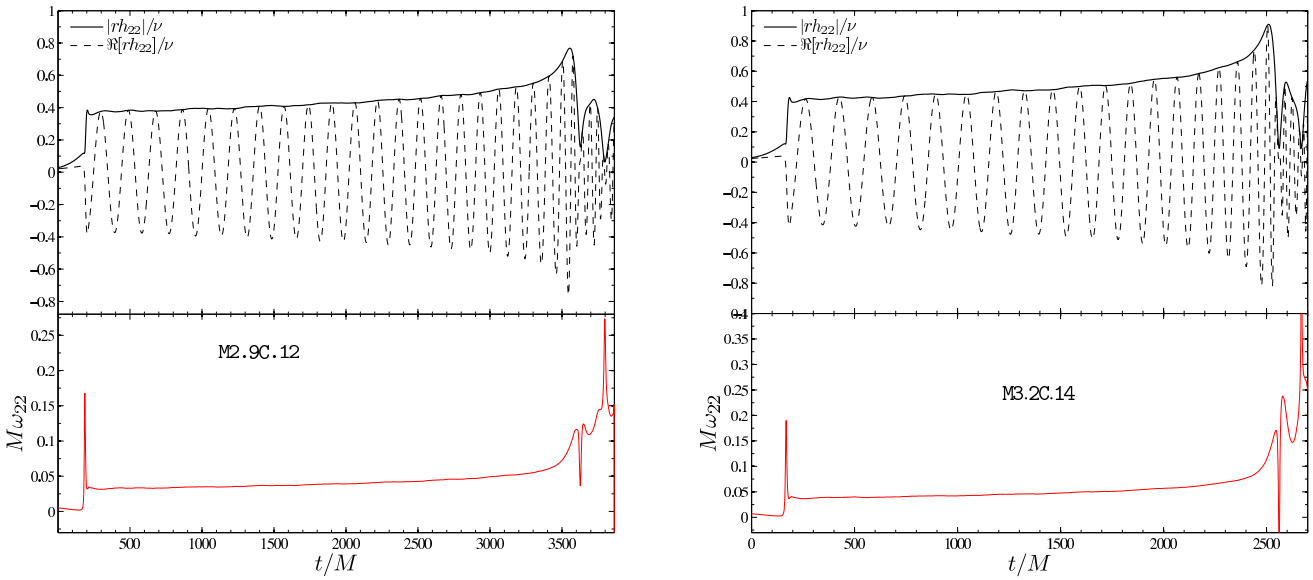

FIG. 2. Metric gravitational waveforms rh_{22} and frequencies (upper panels) and the corresponding istantaneous frequency $M\omega_{22}$ (lower panels) obtained from the (double) time-integration of the curvature waveforms of Fig. 1 [see Eq. (6)]. The left panels refer to model `M2.9C.12`, the right panels to model `M3.2C.14`. The fact that the waveform modulus grows monotonically without evident spurious oscillations is the indication of the reliability of the determination of the integration constants. See text for details.

In order to perform direct comparisons with (resummed) analytical waveforms and since the resummations used in the EOB method have been developed (and tested) mainly for metric waveforms, we derived the metric waveform by a (double) time-integration of the ψ_4^{22} waveform (the so-obtained metric waveform was found to be more accurate than the output of the gauge-invariant perturbation scheme). We recall that the metric waveform is also expanded in spin-weighted spherical harmonics with the following convention

$$h_+ - \mathrm{i}h_\times = \sum_{\ell=2}^{\infty} \sum_{m=-\ell}^{\ell} h_{\ell m}\, {}_{-2}Y_{\ell m}(\theta,\phi), \qquad (5)$$

so that the metric multipoles $h_{\ell m}$ at time t can be obtained from $\psi_4^{\ell m}$ by double time-integration as

$$h_{\ell m}(t) = \int_{-\infty}^{t} dt' \int_{-\infty}^{t'} dt'' \psi_4^{\ell m}(t''). \tag{6}$$

This expression assumes that one knows the curvature waveform on the infinite time interval $(-\infty, t]$. Since, however, the simulated curvature waveform does not start at an infinite time in the past, but at a finite (conventional) time $t = 0$, one has to find a way of determining two (complex) integration constants accounting from the GW emission from infinite time to our present starting time. To do so, we use here an improved version of the fit procedure of Ref. [46], which is presented in detail in Appendix A. Figure 2 shows the result of this process, with the left panels referring to model `M2.9C.12` and the right ones to model `M3.2C.14`. Note that the waveforms displayed in these figures are obtained from simulations with: (i) the non-isentropic (ideal fluid) EOS; (ii) the highest available resolution; and (iii) an extraction radius of $500\,M_\odot$. These will be taken as our fiducial "target" waveforms for our NR/AR comparisons, and we will refer to them in the following with the label $\mathrm{IF_{HR}500}$. The numerical uncertainty on these target waveforms will be estimated in Sec. V below.

III. ANALYTICAL MODELS

We recall below some basic information relative to the EOB-based and PN-based descriptions of the binary dynamics and waveforms that include tidal effects. We follow here the general discussion of Ref. [21], to which we refer the reader for more details. We consider successively: (i) the resummed EOB description of the conservative dynamics, (ii) the resummed EOB description of the waveform, and (iii) one of the non-resummed (i.e., PN expanded) descriptions of the phasing.

A. Effective-one-body description of the conservative dynamics

The EOB formalism [24–26] replaces the PN-expanded two-body interaction Lagrangian (or Hamiltonian) by a resummed Hamiltonian, of a specific form, which depends only on the relative position and momentum of the binary system $(\boldsymbol{q}, \boldsymbol{p})$. For a non spinning BBH system, it has been shown that its dynamics, up to the 3PN level, can be described by the following EOB Hamiltonian (in polar coordinates, within the plane of the motion):

$$H_{\rm EOB}(r, p_{r_*}, p_\varphi) \equiv Mc^2 \sqrt{1 + 2\nu(\hat{H}_{\rm eff} - 1)}\,, \tag{7}$$

where

$$\hat{H}_{\rm eff} \equiv \sqrt{p_{r_*}^2 + A(r)\left(1 + \frac{p_\varphi^2}{r^2} + z_3\,\frac{p_{r_*}^4}{r^2}\right)}\,. \tag{8}$$

Here $M \equiv M_A + M_B$ is the total mass, $\nu \equiv M_A M_B/(M_A + M_B)^2$ is the symmetric mass ratio, and $z_3 \equiv 2\nu(4-3\nu)$. In addition, we are using rescaled dimensionless (effective) variables, namely $r \equiv r_{AB}c^2/GM$ and $p_\varphi \equiv P_\varphi c/(GM_AM_B)$, and p_{r_*} is canonically conjugated to a "tortoise" modification of r [47].

A remarkable feature of the EOB formalism is that the complicated, original 3PN Hamiltonian (which contains many corrections to the basic Newtonian Hamiltonian $\frac{1}{2}\boldsymbol{p}^2 - 1/r$) can be replaced by the simple structure (7)-(8), whose two crucial ingredients are: (i) a "double square-root" structure $H_{\rm EOB} \sim \sqrt{1 + \sqrt{\boldsymbol{p}^2 + \cdots}}$ and (ii) the "condensation" of most of the nonlinear relativistic gravitational interactions in one function of the (EOB) radial variable: the basic "radial potential" $A(r)$. The structure of the function $A(r)$ is rather simple at 3PN, being given by

$$A^{\rm 3PN}(r) = 1 - 2u + 2\,\nu\,u^3 + a_4\,\nu\,u^4\,, \tag{9}$$

where $a_4 = 94/3 - (41/32)\pi^2$, and $u \equiv 1/r = GM/(c^2 r_{AB})$. It was recently found that an excellent description of the dynamics of BBH systems is obtained [27] by: *(i)* augmenting the presently computed terms in the PN expansion (9) by additional 4PN and 5PN terms; *(ii)* Padé-resumming the corresponding 5PN "Taylor" expansion of the A function. In other words, the BBH (or "point mass") dynamics is well described by a function of the form

$$A^0(r) = P_5^1\left[1 - 2u + 2\nu u^3 + a_4\nu u^4 + a_5\nu u^5 + a_6\nu u^6\right], \tag{10}$$

where P_m^n denotes an (n, m) Padé approximant. It was found in Ref. [27] that a good agreement between EOB and numerical-relativity BBH waveforms is obtained in an extended "banana-like" region in the (a_5, a_6) plane approximately spanning the interval between the points $(a_5, a_6) = (0, -20)$ and $(a_5, a_6) = (-36, +520)$. In this work we will select the values $a_5 = -6.37$, $a_6 = +50$, which lie within this region (we have checked that the use of other values within the "good BBH fit" region would have no measurable influence on our discussion below).

The proposal of Ref. [21] for including dynamical tidal effects in the conservative part of the dynamics consists in simply using Eqs. (7)-(8) with the following tidally-augmented radial potential

$$A(u) = A^0(u) + A^{\rm tidal}(u). \tag{11}$$

Here $A^0(u)$ is the point-mass potential defined in Eq. (10), while $A^{\rm tidal}(u)$ is a supplementary "tidal contribution" of the form

$$A^{\rm tidal} = \sum_{\ell \geq 2} -\kappa_\ell^T u^{2\ell+2} \hat{A}_\ell^{\rm tidal}(u)\,, \tag{12}$$

where the terms $\kappa_\ell^T u^{2\ell+2}$ represent the leading-order (LO) tidal interaction, i.e., the Newtonian order tidal interaction. The dynamical EOB tidal coefficients κ_ℓ^T are

functions of the two masses M_A and M_B, of the two compactnesses $\mathcal{C}_{A,B} = GM_{A,B}/R_{A,B}$, and of the two (relativistic) Love numbers $k_\ell^{A,B}$ of the two objects [18–20]:

$$\kappa_\ell^T = 2\frac{M_B\, M_A^{2\ell}}{(M_A+M_B)^{2\ell+1}}\frac{k_\ell^A}{\mathcal{C}_A^{2\ell+1}} + \{ {}_A \leftrightarrow {}_B\} = \frac{1}{2^{2\ell-1}}\frac{k_\ell}{\mathcal{C}^{2\ell+1}}\,, \tag{13}$$

where the second line refers to an equal-mass binary, as the ones considered here. Note in Table I the rather large numerical values for the $\ell = 2$ tidal coefficients: $\kappa_2^T(\mathcal{C} = 0.12) \simeq 496$ and $\kappa_2^T(\mathcal{C} = 0.14) \simeq 184$. In our EOB modelling we also use the higher multipolar tidal coefficients κ_3^T and κ_4^T, which are even larger than κ_2^T (e.g., $\kappa_4^T(\mathcal{C} = 0.12) \simeq 20318$), although their effect is marginal in view of the higher power of u (namely $u^{2\ell+2}$) with which they enter the $A(r)$ potential.

The additional factor $\hat{A}_\ell^{\rm tidal}(u)$ in Eq. (12) represents the effect of higher-order relativistic contributions to the dynamical tidal interactions: next-to-leading–order (NLO) contributions, next-to-next-to-leading–order (NNLO) contributions, etc. Here we will consider a "Taylor-expanded" expression

$$\hat{A}_\ell^{\rm tidal}(u) = 1 + \bar{\alpha}_1^{(\ell)} u + \bar{\alpha}_2^{(\ell)} u^2\,, \tag{14}$$

where $\bar{\alpha}_n^{(\ell)}$ are functions of M_A, $\mathcal{C}_A$, and k_ℓ^A for a general binary. The analytical value of the ($\ell = 2$) 1PN coefficient $\bar{\alpha}_1^{(2)}$ has been reported in [21] (and recently confirmed in [48]). In the equal-mass case, it yields $\bar{\alpha}_1^{(2)} = 1.25$. By contrast, there are no analytical calculations available for $\bar{\alpha}_1^{(\ell)}$ with $\ell > 2$, nor for the 2PN tidal coefficients $\bar{\alpha}_2^{(\ell)}$. Indeed, one of the main aims of the present work will be to constrain the value of $\bar{\alpha}_2^{(2)}$ by comparing the EOB predictions to numerical data.

B. Effective-one-body description of the waveform and radiation reaction

Let us first recall that the EOB formalism defines the radiation reaction from the angular-momentum flux computed from the waveform. Concerning the waveform, in the case of BBH systems, the EOB formalism replaces the PN-expanded multipolar (metric) waveform $h_{\ell m}^{\rm PN}$ by a specifically resummed "factorized waveform" [31, 49], say $h_{\ell m}^0$ (where the superscript 0 is added to signal the absence of tidal effects). This tidal-free multipolar waveform $h_{\ell m}^0$ includes resummed versions of very high-order PN effects in the phase and the modulus, in particular *tail effects*. Actually, in the present work, we have used a factorized waveform which includes in the modulus (but not in the phase) the new (5PN accurate) $\nu = 0$ terms recently computed in [50][3]. We also included in $h_{\ell m}^0$ the two next-to-quasi-circular parameters (a_1, a_2) as in Ref. [27][4].

When considering tidally interacting binary systems, one needs to augment the BBH waveform $h_{\ell m}^0$ by tidal contributions. Similarly to the additive tidal modification (11) of the A potential, we will here consider an *additive* modification of the waveform, having the structure

$$h_{\ell m} = h_{\ell m}^0 + h_{\ell m}^{\rm tidal}\,. \tag{15}$$

This is slightly different from the factorized form introduced in Eq. (71) of [21] and used in [1]. The above additive form turns out to be more convenient for incorporating higher-order relativistic corrections to the tidal waveform. Using the recent computation [29] of the 1PN-accurate Blanchet-Damour mass quadrupole moment [51] of a tidally interacting binary system (together with the Newtonian-accurate spin quadrupole and mass octupole) and transforming their symmetric-trace-free tensorial results into our ℓm-multipolar form, we have computed the corresponding 1PN-accurate value[5] of $h_{22}^{\rm tidal}$, as well as the 0PN-accurate values of $h_{21}^{\rm tidal}$, $h_{33}^{\rm tidal}$, and $h_{31}^{\rm tidal}$. In addition, using the general analysis of tail effects in Refs. [30, 52] and the resummation of tails introduced in Refs. [31, 53], we were able to further improve the accuracy of these waveforms by incorporating (in a resummed manner) the effect of tails (to all orders in M). From a PN point of view, this means, in particular, that the tidal contribution we use to the total metric waveform is 1.5PN accurate.

In summary, the EOB tidal model that we use here is analytically complete at the 1.5 PN level. In addition, we adopt the simplifying assumption that the higher–multipolar tidal–amplification factors $\hat{A}_\ell^{\rm tidal}(u)$, for $\ell > 2$, are taken to coincide with the $\ell = 2$ one. This means that the EOB model that we will use here contains *only one* (yet undetermined) higher-order flexibility parameter, say $\bar{\alpha}_2$, that is taken to replace the various $\bar{\alpha}_2^{(\ell)}$, with $\ell = \{2, 3, 4, \dots\}$, entering Eq. (14), i.e. $\bar{\alpha}_2^{(\ell)} \equiv \bar{\alpha}_2$ (and, similarly, $\bar{\alpha}_1^{(\ell)} = \bar{\alpha}_1^{(2)} \equiv \bar{\alpha}_1$). Note that, although this parameter is formally of 2PN order, it is used here as an *effective* parametrization of all the higher-order effects not covered by the current analytical knowledge (both in the conservative dynamics and in the radiation reaction).

---

[3] As in Ref. [49] we resum the $\ell = 2, m = 2$ modulus by using the Padé-resummed function $f_{22}^{\rm Pf}(x;\nu) = P_2^3[f_{22}^{\rm Taylor}(x;\nu)]$.

[4] Since both `M2.9C.12` and `M3.2C.14` are equal-mass binaries, we fix $a_1 = -0.0439$ and $a_2 = 1.3077$, according to the EOB/NR comparison (for a BBH equal-mass system) of Ref. [27].

[5] We leave a detailed presentation of our results to future work. Let us however mention that, notwithstanding some statements in footnote 4 of [29], the 1PN-accurate (circular) quadrupolar waveform exactly matches the form given in Eq. (71) of [21] (which was expressed in terms of frequency-related gauge-invariant quantities).

Note also that, while in the general case such a parameter should be allowed to depend on the mass ratio and the compactnesses, in the equal-mass case that we consider here, it is a pure number. We will use below the comparison between NR simulations and EOB predictions to constrain the value of the effective higher-order parameter $\bar{\alpha}_2$.

C. PN-expanded Taylor-T4

Tidal effects can be accounted for also via modifications of one of the non-resummed PN description of the dynamics of inspiralling binaries [7, 16, 20]. Reference [20], in particular, has recently suggested to use as baseline a time-domain T4-type incorporation of tidal effects. We recall that the phasing of the T4 approximant is defined by the following equations

$$\begin{aligned} \frac{d\phi_{22}^{\rm T4}}{dt} &= 2\,x^{3/2}, \\ \frac{dx}{dt} &= \frac{64}{5}\,\nu\,x^5\,\left\{a_{3.5}^{\rm Taylor}(x)+a^{\rm tidal}(x)\right\}\,, \end{aligned} \tag{16}$$

where $a_{3.5}^{\rm Taylor}$ is the PN expanded expression describing point-mass contributions, given by

$$\begin{aligned} a_{3.5}^{\rm Taylor}(x) &= 1-\left(\frac{743}{336}+\frac{11}{4}\nu\right)x+4\pi x^{3/2} \\ &+\left(\frac{34103}{18144}+\frac{13661}{2016}\nu+\frac{59}{18}\nu^2\right)x^2-\left(\frac{4159}{672}+\frac{189}{8}\nu\right)\pi x^{5/2} \\ &+\left[\frac{16447322263}{139708800}-\frac{1712}{105}\gamma-\frac{56198689}{217728}\nu+\frac{541}{896}\nu^2\right. \\ &\left.-\frac{5605}{2592}\nu^3+\frac{\pi^2}{48}(256+451\nu)-\frac{856}{105}\ln(16x)\right]x^3 \\ &+\left(-\frac{4415}{4032}+\frac{358675}{6048}\nu+\frac{91495}{1512}\nu^2\right)\pi x^{7/2} \end{aligned} \tag{17}$$

and where $a^{\rm tidal}$ is the tidal contribution. From [29] the latter is given at 1PN accuracy by

$$a^{\rm tidal}(x)=\sum_{I=A,B}a_{\rm LO}(X_I)x^5(1+a_1(X_I)x)\,, \tag{18}$$

with

$$a_{\rm LO}(X_I)=4\hat{k}_2^I\frac{12-11X_I}{X_I} \tag{19}$$

and

$$a_1(X)=\frac{4421-12263X+26502X^2-18508X^3}{336(12-11X)}, \tag{20}$$

where we introduced the auxiliary quantity

$$\hat{k}_2^I\equiv k_2^I\left(\frac{X_I}{\mathcal{C}_I}\right)^5 \qquad I=A,B. \tag{21}$$

In the particular case of equal-mass binaries, $X_A=X_B=X=1/2$, $\mathcal{C}_A=\mathcal{C}_B=\mathcal{C}$, and the tidal contribution $a^{\rm tidal}(x)$ has the form

$$a^{\rm tidal}(x)=26\,\kappa_2^T x^5\,(1+a_1^{\rm T4}x), \tag{22}$$

with $a_1^{\rm T4}=5203/4368\approx 1.19$.

Similarly to the inclusion of yet undetermined higher-order effects in the tidally-augmented EOB formalism via the effective parameter $\bar{\alpha}_2$, we will consider below an *effective* modification of the 1PN result (22) of the form

$$a^{\rm tidal}(x)=26\,\kappa_2^T x^5\,(1+a_1^{\rm T4}x+a_2^{\rm T4}x^2), \tag{23}$$

with an effective higher-order parameter[6] $a_2^{\rm T4}$, which we will constrain by comparing NR data to the T4-predicted phasing.

Let us mention that, in the case of inspiralling BBH systems, several studies [31, 46, 54] have shown that the nonresummed Taylor-T4 description of the GW phasing was significantly less accurate than the EOB description, especially for mass ratios different from one. Ref. [21] has also shown that, in the presence of tidal effects, it was predicting GW phases that differed by more than a radian with respect to the tidal-completed EOB model. Below, we will investigate how the T4 phasing based on Eq. (16) differs from the EOB one, both in the absence (Eq. (22)) and in the presence (Eq. (23)) of the higher-order parameter $a_2^{\rm T4}$.

IV. CHARACTERIZING THE PHASING: THE $Q_\omega(\omega)$ FUNCTION

In order to measure the influence of tidal effects it is useful to consider the "phase acceleration"[7] $\dot{\omega}\equiv d\omega/dt\equiv d^2\phi/dt^2$ as a function of ω, say $\dot{\omega}=\alpha(\omega)$ (here $\omega\equiv\omega_{22}$ can be either the curvature or the metric instantaneous GW frequency). Indeed, as emphasized in [31], the function $\alpha(\omega)$ is independent of the two "shift ambiguities" that affect the GW phase $\phi(t)$, namely the shifts in time and phase. The $\alpha(\omega)$ diagnostics (especially in its Newton-reduced form $a_\omega=\alpha(\omega)/(c_\nu\omega^{11/3})$, with $c_\nu=\frac{12}{5}2^{1/3}\nu$, is a useful intrinsic measure of the quality of the waveform and it has been used extensively in recent analyses of BBHs [46, 53, 55, 56].

Here we will use another dimensionless measure of the phase acceleration: the function $Q_\omega(\omega)$. It is defined as

[6] We found that the 1.5PN fractional contribution $a_{3/2}^{\rm T4}x^{3/2}$ to $a^{\rm tidal}(x)$, predicted by our 1.5PN-accurate EOB waveform, has (like the 1PN contribution) only a small effect on the phasing compared to the large amplification that we will need to agree with NR data. This is why we only consider here, for simplicity and for easier comparison with the 2PN EOB parameter $\bar{\alpha}_2$, the formally 2PN parameter $a_2^{\rm T4}$.

[7] In the text of this Section t and ω denote the dimensionless quantities $\hat{t}\equiv t/M$ and $\hat{\omega}\equiv M\omega$.

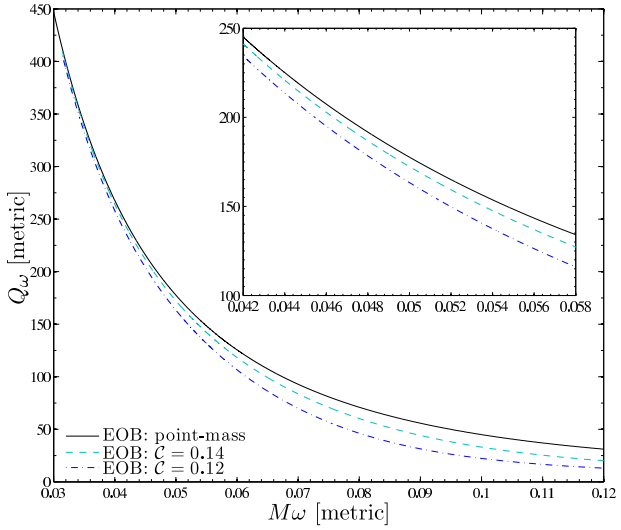

FIG. 3. Exploring the properties of Q_ω curves computed within the EOB model for three binary systems. Tidal interactions are approximated at LO. The inset shows a magnification, in order to highlight the differences among the curves.

the derivative of the (time-domain) phase with respect to the logarithm of the (time-domain) frequency:

$$Q_\omega(\omega) = \frac{d\phi}{d\,\ln\,\omega} = \frac{\omega\, d\phi/dt}{d\omega/dt} = \frac{\omega^2}{\dot\omega} = \frac{\omega^2}{\alpha(\omega)}\,. \qquad (24)$$

Note that, as a consequence of this definition, the (time-domain) GW phase $\phi_{(\omega_1,\omega_2)}$ accumulated between frequencies (ω_1, ω_2) is given by the following integral:

$$\phi_{(\omega_1,\omega_2)} = \int_{\omega_1}^{\omega_2} Q_\omega d\ln\omega\,. \qquad (25)$$

Stated differently, the function $Q_\omega(\omega)$ measures the number of GW cycles spent by the binary system within an octave of the GW frequency ω (it is therefore analogous to the "quality factor" Q of a damped oscillator). Let us also note that, in the stationary phase approximation, Q_ω enters as an amplification factor of the signal, so that the squared signal-to-noise ratio is equal to [57]

$$\rho^2 = 4\int d\ln\,\omega\,\frac{Q_\omega(\omega)\,A^2(\omega)}{\omega\,S_n(f)}\,, \qquad (26)$$

where A denotes the amplitude of the time-domain metric waveform and where $S_n(f)$ denotes the one-sided noise power spectral density and $f \equiv \omega/(2\pi)$.

In view of its definition, Q_ω is a useful *quantitative indicator* of the physics driving the variation of ω. Indeed, a change of $Q_\omega(\omega)$ of the order ±1 during a frequency "octave" $\ln(\omega_2/\omega_1) = 1$ corresponds to a local dephasing (around ω) of $\Delta\phi \simeq \pm1$ rad. Because such a dephasing (if it occurs within the sensitivity band of the detector) can be expected to significantly affect the measurability of the signal, it is probably necessary to model Q_ω with an absolute accuracy of about ±1 (see Ref. [55] for a quantitative discussion of the admissible error level on Q_ω in the BBH context).

We start our analysis by comparing the Q_ω functions (as predicted by the EOB formalism) for the (metric) gravitational waveforms h_{22} generated by three (equal-mass) binary models, namely a BBH and the two BNS systems discussed in Sec. II A. To simplify the discussion, these functions are computed with the LO tidal interaction $\hat{A}_\ell(u) = 1$. [We will separately study below the effect of changing $\hat{A}_\ell(u)$.]

Figure 3 compares the properties of the Q_ω functions by showing together the curves for the three binaries versus their corresponding GW frequency. A number of remarks are worth making. First, Q_ω is a large number that diverges in the small-frequency limit. This follows from the fact that in the limit $\omega \to 0$ one has $\alpha(\omega) \sim c_\nu \omega^{11/3}$, and then, via Eq. (24), $Q_\omega = 1/(c_\nu\omega^{5/3}) \sim (c/v)^5$. Second, the presence of tidal interactions *decreases* the "point-mass" value of Q_ω by an amount that is (essentially) proportional to κ_2^T. In other words, tidal effects "accelerate" the inspiral by reducing the number of cycles spent around a given frequency. In particular, BBHs (which have vanishing tidal constants [18, 19]) are effectively the binaries that spend the largest time at any given frequency. Finally, note that since Q_ω is a large number, the fact that the curves look relatively close on the large-scale plot can be misleading, since the corresponding accumulated relative phase difference can actually be large (see inset, which shows that the absolute differences between the various $Q_\omega(\omega)$ is of order 10, corresponding to integrated dephasings of order 10 radians).

Although the calculation of the phase "quality-factor" Q_ω is straightforward within the EOB framework, this is not the case when Q_ω is to be calculated from the NR (either curvature or metric) waveforms. Indeed, the direct computation of the Q_ω functions from raw data is in general made difficult by the presence of both high-frequency noise in $\omega(t)$ and of low-frequency oscillations probably due to a residual eccentricity. This is illustrated in the right panels of Fig. 4, where we show with (light) dashed lines the raw NR Q_ω functions obtained by direct time-differentiation of the NR curvature (top panel) or metric (bottom panel) phase for the binary `M3.2C.14`. A fourth order accurate finite differencing algorithm has been used to compute the derivatives. Similar results have been obtained also for the binary `M2.9C.12`.

The right panel of Fig. 4 shows that the two time-derivatives involved in the definition of $Q_\omega(\omega)$ amplify considerably the high-frequency noise contained in the NR phase evolution, and make it impossible to extract a reliable value of $Q_\omega(\omega)$ from such a *direct* numerical attack. To tackle this problem, one needs to filter out the high-frequency numerical errors in the time-domain phase before effecting any time-differentiation. To do this, we found useful to "clean" the phase $\phi(t)$ by fitting the NR phase to an analytic expression that is inspired by the PN expansion. More precisely, after introducing

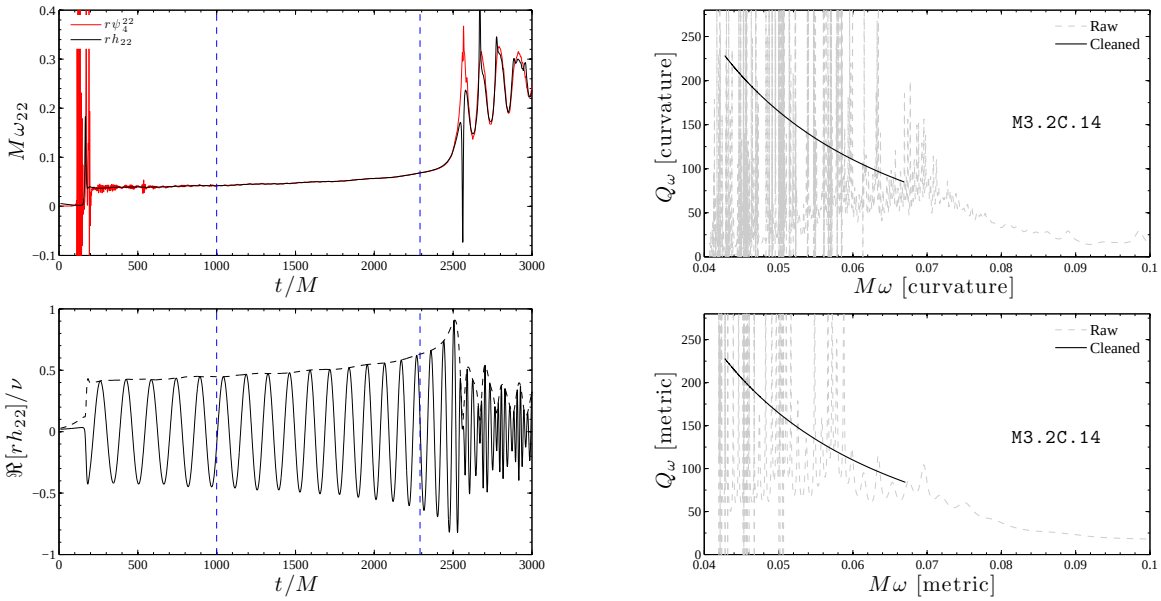

FIG. 4. Obtaining the Q_ω diagnostic from a suitable fitting procedure of the GW phase (for both curvature and metric waveforms). The two vertical lines on the left panels indicate the time interval $\Delta t/M = [1000, 2290]$ where we fit the NR phase with Eq. (28). For completeness we also display the real part of the metric waveform. On the right panels, the (light) dashed lines refer to the Q_ω obtained by direct numerical differentiation of the raw data; the solid lines are instead obtained from the fitted phase. Although the curves displayed here refer to model `M3.2C.14`, similar results are obtained also for the binary `M2.9C.12`.

a formal "coalescence" time t_c and defining the quantity

$$x \equiv \left[\frac{\nu}{5}(t_c - t)\right]^{-1/8} , \tag{27}$$

we fitted the time-domain NR phase $\phi^{\rm NR}(t)$ to an expression of the form

$$\phi(t; t_c, p_2, p_3, p_4, \phi_0) = \phi_0 + -\frac{2}{\nu}x^{-5} \times \left(1 + p_2 x^2 + p_3 x^3 + p_4 x^4\right) . \tag{28}$$

In this expression, we have set the lower coefficients p_0 and p_1 to $p_0 = 1$ and $p_1 = 0$, as suggested by the corresponding lowest-order PN expression (see, e.g., Eq. (234) of [58]), but we left t_c, ϕ_0, and the higher-PN p_i's as free coefficients to be determined from the NR data. The basic idea is that of using a simple analytical form that incorporates the leading trend of Q_ω to remove the influence of the numerical errors while leaving some flexibility in the subleading part of the phase evolution that is influenced by tidal effects. We view the fitting parameters p_2, p_3, p_4 as effective parameters for describing tidal-phasing effects.

Such a fit of the phase evolution can be reliably done only in a limited time interval. Indeed, one has to cut off both the early phase of the inspiral (where the numerical data is too noisy), and the last few cycles before the merger (where the PN-based fit is no longer a good approximation). We present in Appendix B a detailed discussion of the optimal choice of the time interval where to make the fit, as well as a series of consistency checks. See also the discussion at the end of Sec. V B.

Let us start by discussing the application of this procedure to the GW phase (both curvature and metric) of the binary model `M3.2C.14`. The result of this fitting is shown by the solid lines in the right-panels of Fig. 4 (top, curvature phase; bottom, metric phase). The time interval on which we could reliably apply the fitting procedure is $I_t/M = [1000, 2290]$. This time window is indicated by the dashed vertical lines in the top-left panel of Fig. 4, were we show together the time evolution of both the curvature (dashed, red online) and metric (solid) GW frequencies. For completeness, the lower-left panel of the same figure translates this information in terms of GW cycles of the metric waveform. Note that this time interval excludes the first 4 GW cycles (whose NR frequency is indeed seen to be quite noisy), but covers about 10 GW cycles, and ends around 2 GW cycles before the merger (defined as the maximum of the modulus of the metric waveform; the modulus of the metric waveform is indicated by a dashed line on the left-bottom panel of the figure). The corresponding frequency interval can be visualized on the right panels, and is listed in the fifth column of Table III. Similar results are obtained also

for the M2.9C.12 data (see Fig. 10 below). In this case, the time interval we use is $I_t/M = [1300, 3366]$, with the corresponding frequencies listed in the seventh column of Table III. Finally, notice that for this model the inspiral is longer than in the previous case and so this interval actually corresponds to 14 GWs cycles. In addition, similarly to the other case, our choice of fitting interval excludes the first 5.5 GW cycles, and ends about 2 GW cycles before merger.

As we will discuss below, although the frequency windows where our cleaning procedure allowed us to compute an estimate of the NR $Q_\omega(\omega)$ functions do not cover the full inspiral, these estimates will give us access to important information for performing quantitative comparisons with the predictions of the EOB (and Taylor T4) analytical models.

V. NUMERICAL ERROR-BUDGET

The aim of this section is to discuss the various errors affecting the numerical waveforms extracted (for both models) at $500\,M_\odot$ and computed with the highest resolution. Such a discussion will in turn allow us to estimate an uncertainty range on the analytical parameter $\bar{\alpha}_2$ representing the not-yet-calculated, high-PN-order tidal effects entering the EOB description of the phasing.

We will discuss in turn the numerical errors entailed by three different effects: (i) the choice of EOS (isentropic versus non-isentropic evolution); (ii) the finite extraction radius; (iii) the finite resolution. We will perform this analysis both by comparing waveforms in the time domain and by means of the Q_ω diagnostic.

A. Time-domain analysis

1. *Non-isentropic evolutions*

As discussed in Sec. II A, we have evolved the binaries using either a (isentropic) polytropic EOS or a (non-isentropic) ideal-fluid EOS. We recall that, in the absence of large-scale shocks (like those taking place at the merger), the two EOSs are equivalent and should therefore yield evolutions that differ only at machine precision. In practice, however, when using the ideal-fluid EOS small shocks are produced in the very low-density layers of the stars even when these orbit [2]. These small shocks channel some of the orbital kinetic energy into internal energy, leading to small ejections of matter (i.e., amounting to a total of $\sim 10^{-6} M_\odot$), and are thus responsible for slight differences even during the inspiral. Since we are here presenting the results of simulations that are considerably longer than any presented so far and in particular of those in Refs. [2, 6], it is important to quantify the influence of these non-isentropic effects. Concentrating on model M3.2C.14, we show in the top-panel of Fig. 5 the real parts of the $r\psi_4^{22}$ waveforms computed with the two EOSs as extracted at $r_{\rm obs} = 500 M_\odot = 165.1M$. The bottom panel displays the corresponding instantaneous frequencies for completeness. As customary in comparing waveforms in the time domain, one allows for arbitrary relative time and phase shifts (τ, α). These quantities can be determined in various ways, for example by means of the two-frequency pinching technique of Ref. [59]. In this paper we find it useful to use the method used in Ref. [54] to compute (τ, α). More precisely, given two timeseries of the phase $\{\phi_1(t_i), \phi_2(t_i)\}$ defined on a given time interval $[t_L, t_R]$ that is covered by N numerical points t_i, with $i = 1, 2, \ldots, N$, we define the quantity

$$\Delta\phi(t_i, \tau, \alpha) = \phi_2(t_i + \tau) - \phi_1(t_i) - \alpha \qquad (29)$$

and determine τ and α such that they minimize the "reduced" χ^2 quantity

$$\widehat{\chi}^2 = \frac{1}{N} \sum_{i=1}^{N} (\Delta\phi(t_i, \tau, \alpha))^2. \qquad (30)$$

The minimization on α is done analytically, while that on τ is done numerically. Note in addition that the square root of the minimum value of Eq. (30), say

$$\sigma_{\Delta\phi} = \sqrt{\frac{1}{N} \sum_{i=1}^{N} (\Delta\phi(t_i, \tau, \alpha))^2_{\rm min}} \qquad (31)$$

has the meaning of a root-mean-square deviation of the phase difference $\Delta\phi$ over the interval $[t_L, t_R]$; as such,

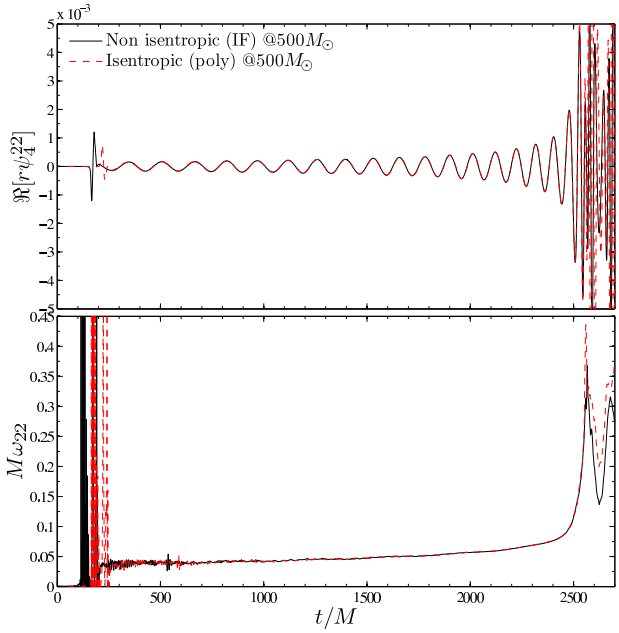

FIG. 5. Comparing waveforms from isentropic (dashed) and non-isentropic (solid) evolution for BNS model M3.2C.14. Waveforms are computed with the highest resolution and extracted at $r_{\rm obs} = 500\,M_\odot$. The corresponding phase difference $\phi^{\rm poly_{HR}500} - \phi^{\rm IF_{HR}500}$ is displayed in Fig. 6.

it can also be employed to give a quantitative measure of a phase difference (and thereby of some phase errors).[8] The phase difference $\Delta\phi(t) \equiv \phi_2(t) - \phi_1(t) = \phi^{\mathrm{poly}_{\mathrm{HR}}500} - \phi^{\mathrm{IF}_{\mathrm{HR}}500}$ (least-square minimized on the time interval $[t_L, t_R]/M = [300, 2540]$) is represented as a dash-dotted line (solid light blue) in Fig. 6. One sees that the instantaneous phase difference varies roughly between $+0.2$ rad and -0.1 rad on this time interval, which corresponds to a "two-sided" [59] phase uncertainty of the order $\Delta\phi = \pm\frac{1}{2}(0.2 - (-0.1)) = \pm 0.15$ rad. The information of Fig. 6 is completed by Table II, where we list the ℓ^∞ norm of the phase difference [i.e., the maximum absolute value of $\Delta\phi(t)$], labelled $||\Delta\phi||^\infty$, the root-mean-square $\sigma_{\Delta\phi}$ as computed above, and the corresponding time interval $[t_L, t_R]$ that is used to compute (α, τ). Note that $\sigma_{\Delta\phi}$ gives a measure of the phase difference which is always significantly smaller than the ℓ^∞ norm. Indeed, these two quantities measure different aspects of a phase difference, and, when the time variation of $\Delta\phi(t)$ is dominated by low-frequency effects (which can be roughly modelled as power laws), the averaging involved in the definition of $\sigma_{\Delta\phi}$ will lead to a smallish ratio $\sigma_{\Delta\phi}/||\Delta\phi||^\infty < 1$ linked to integrals of the type $\int_0^1 dt\, t^{2n} = 1/(2n+1)$.

2. *Finite-radius extraction*

We next discuss the phasing error introduced by the fact that our high-resolution target waveforms, for both models, are extracted at the finite coordinate radius $r_{\mathrm{obs}} = 500\,M_\odot$. Note that, when expressed in units of the gravitational mass M of the binary at infinite separation, this value corresponds to $r_{\mathrm{obs}} = 134.9M$ for `M2.9C.12` and $r_{\mathrm{obs}} = 165.1M$ for `M3.2C.14`, i.e., , for one model waves are actually extracted slightly farther than for the other. For both models we have at our disposal several extraction radii, so that we can estimate the phasing error linked to the finite extraction radius as follows: (i) We used the raw $r\psi_4^{22}$ data extracted at radii $r = \{400, 450, 500\}\,M_\odot$; (ii) We time-shifted them so that this triplet of timeseries is expressed as a function of the (coordinate) retarded time $t_* = t - r - 2M_{\mathrm{ADM}} \ln[r/(2M_{\mathrm{ADM}}) - 1]$; (iii) We separated each curvature waveform in phase and amplitude as functions of $u \equiv 1/r$ (cf. page 6); (iv) We fitted each resulting triplet of timeseries to a linear polynomial in the triplet of inverse extraction radii: $c^\infty(t_*) + c_1(t_*)/r$.

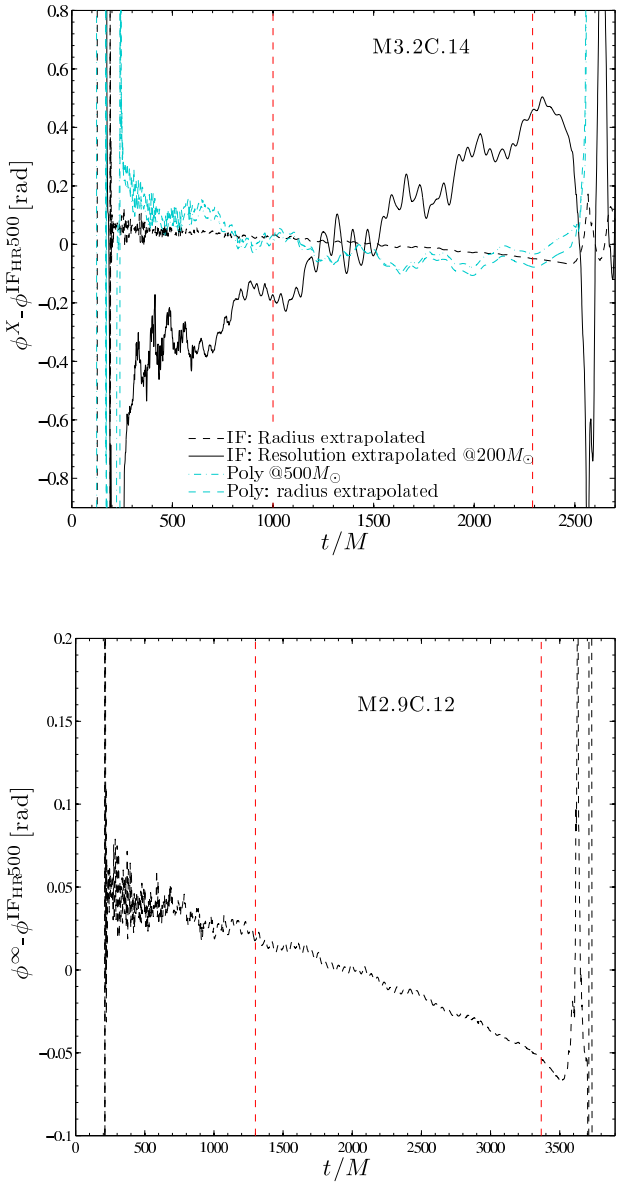

FIG. 6. Estimate of the phase uncertainty in the time domain for model `M3.2C.14` (top) and `M2.9C.12` (bottom). The figure shows the phase difference between different "post-processed" numerical curvature waveforms $r\psi_4^{22}$ (in particular, extrapolated in resolution and/or extraction radius) and the one obtained with the ideal-fluid EOS and extracted at $r_{\mathrm{obs}} = 500\,M_\odot$.

The quantities $c^\infty(t_*)$ [i.e., $A^\infty(t_*)$ and $\phi^\infty(t_*)$] yield estimates of the amplitude and phase of the infinite-radius extrapolation of $r\psi_4^{22}$. We then compare the radius-extrapolated phase $\phi^\infty(t_*)$ to the phase extracted at the outermost radius, allowing for additional time and phase shifts (which are determined by the least-square minimization discussed above).

The time evolution of the phase differences computed in this way are shown in Fig. 6 for model `M3.2C.14` (top

[8] We note in passing that the alignment procedure also highlights the weak dependence on the EOS of the late part of the waveform: although the inspiral of the non-isentropic waveform is about $150M$ longer than the corresponding isentropic one, the growth of $M\omega_{22}$ (and the corresponding phasing) is qualitatively and quantitatively very close for both models until $M\omega_{22}$ peaks for the first time.

TABLE II. Uncertainty estimates on the phase (in radians) of $r\psi_4^{22}$, computed in the time domain, for both models. From left to right, the columns report: the model name, the EOS, the coordinate extraction radius, the type of extrapolation that is performed on the waveform (either in extraction radius or resolution), the time interval on which the χ^2 of the phase difference is minimized, the ℓ^∞ norm of the phase difference over this interval, and the root-mean-square of the phase difference.

Model	EOS	$r_{\rm obs}$ $[M_\odot]$	Extrap.	$[t_L, t_R]$ $[M]$	$\|\|\Delta\phi\|\|^\infty$ [rad]	$\sigma_{\Delta\phi}$ [rad]
`M3.2C.14`	IF	500	radius	$[400, 2650]$	0.17	0.035
`M3.2C.14`	IF	200	resolution	$[400, 2650]$	1.29	0.300
`M3.2C.14`	poly	500	–	$[300, 2540]$	0.21	0.057
`M3.2C.14`	poly	500	radius	$[300, 2550]$	0.43	0.080
`M2.9C.12`	IF	500	radius	$[250, 3650]$	0.31	0.035

panel, dash-line) and for `M2.9C.12` (bottom panel). This local information is completed by the "global" quantitative information ($||\Delta\phi||^\infty$, $\sigma_{\Delta\phi}$) listed in the last two columns of Table II. On the basis of this analysis, we estimate that, for both models, the phase uncertainty due to finite extraction is of order $\Delta\phi \approx \pm 0.05$ rad almost up to the merger, i.e., roughly $100\,M$ before the peak of the GW frequency.

3. *Finite-resolution error*

Finite-resolution errors have already been discussed in detail in our previous work [6], which used the same numerical setup (i.e., the same resolution and grid structure) adopted here. Skipping the details, we recall that it was shown there that, at the resolution that we are using in this work, the dynamics and waveforms are in a convergent regime, with a convergence rate σ that is $\simeq 1.8$ during the inspiral phase and drops to $\simeq 1.2$ after the merger, when large-scale shocks appear. As the computational cost of the calculations presented here is already at the limit of what can be reasonably afforded, we have decided to estimate the truncation-error of our present waveform by assuming that the inspiral convergence rate $\sigma \simeq 1.8$ found in our previous work [6] approximately holds in the present (numerically similar) case. We have then selected the more compact binary `M3.2C.14` and used only two simulations with different resolutions. More specifically, we have considered a "high-resolution" simulation, where the finest refinement level has a resolution $\Delta_{\rm H} = 0.12\,M_\odot$, and a "low-resolution" simulation, with $\Delta_{\rm L} = 0.15\,M_\odot$. For this particular comparison the waveforms are extracted at $r_{\rm obs} = 200\,M_\odot$. When comparing the low- and high-resolution curvature waveforms, after suitable (τ, α) alignment, one discovers that the phase difference accumulated between the two resolutions over a timescale of $2300M$ during the inspiral is about 0.45 rad (corresponding to a relative error of $\simeq 0.36\%$). Using the convergence rate discussed above, we can now Richardson-extrapolate the results obtained with the two resolutions and obtain an estimate of the "infinite-resolution" waveform. More precisely, we model the suitably aligned, low- and high-resolution phase evolutions as

$$\phi_{\Delta_{\rm H}}(t) = \phi_0(t) + k(t)(\Delta_{\rm H})^\sigma, \tag{32}$$

$$\phi_{\Delta_{\rm L}}(t) = \phi_0(t) + k(t)(\Delta_{\rm L})^\sigma, \tag{33}$$

where $\phi_0(t)$ represents the infinite-resolution phase ($\Delta \to 0$). From the above equations, we obtain the following estimate of the infinite-resolution extrapolation of the phase evolution

$$\phi_0(t) = \frac{(\Delta_{\rm L})^\sigma \phi_{\Delta_{\rm H}}(t) - (\Delta_{\rm H})^\sigma \phi_{\Delta_{\rm L}}(t)}{(\Delta_{\rm L})^\sigma - (\Delta_{\rm H})^\sigma}\,. \tag{34}$$

We performed the same extrapolation also on the waveform modulus, so as to have access to the complete extrapolated curvature waveform. The solid line in Fig. 6 displays the phase difference $\phi_0^{\rm IF200} - \phi^{{\rm IF}_{\rm HR}500}$. This indicates a phase uncertainty of $\Delta\phi \approx \pm 0.5$ rad on $\phi^{{\rm IF}_{\rm HR}500}$ as measured up to about $100M$ before the maximum of $M\omega_{22}$. See Table II for the corresponding global measures of the phase uncertainty, $||\Delta\phi||^\infty$ and $\sigma_{\Delta\phi}$. Note that these uncertainty estimates are much larger than those normally computed for binary BH simulations for the same computational costs (see, for instance, [60]). This is the natural consequence of the smaller resolution employable here and of the lower-order convergence that one achieves when solving the hydrodynamics equations. Since this error is deduced only after *assuming* a certain convergence order (in addition obtained from a slightly different numerical setup) it will be used below only to estimate a rough uncertainty range on the value of the higher-order EOB tidal correction parameter $\bar{\alpha}_2$. We will comment more on this in the next Sections.

Adding in quadrature the various uncertainties computed so far to obtain a total error bar on the phases of the ${\rm IF}_{\rm HR}500$ data for the `M3.2C.14` model would give a (two-sided) time-domain phase uncertainty $\Delta\phi \simeq \pm\sqrt{0.15^2 + 0.05^2} \simeq \pm 0.16$ rad, when excluding the uncertainty due to the finite resolution, or $\Delta\phi \simeq \pm\sqrt{0.15^2 + 0.05^2 + 0.5^2} \simeq \pm 0.52$ rad when including it. Alternatively, if we add in quadrature the root-mean-squares of the corresponding phase errors we find $\sigma_{\Delta\phi} \simeq \pm 0.07$ rad, when excluding the uncertainty due to the finite resolution, and $\sigma_{\Delta\phi} \simeq \pm 0.32$ rad when including it. Clearly the resolution-extrapolation error is dominating the error budget. In view of the uncertainty in estimating this source of error, we will not directly use these time-domain phase-error levels in estimating the uncertainties in the comparison between the EOB, T4, and NR phasings. As we will discuss next, we prefer to express the information gathered above on numerical errors in terms of the corresponding Q_ω curves.

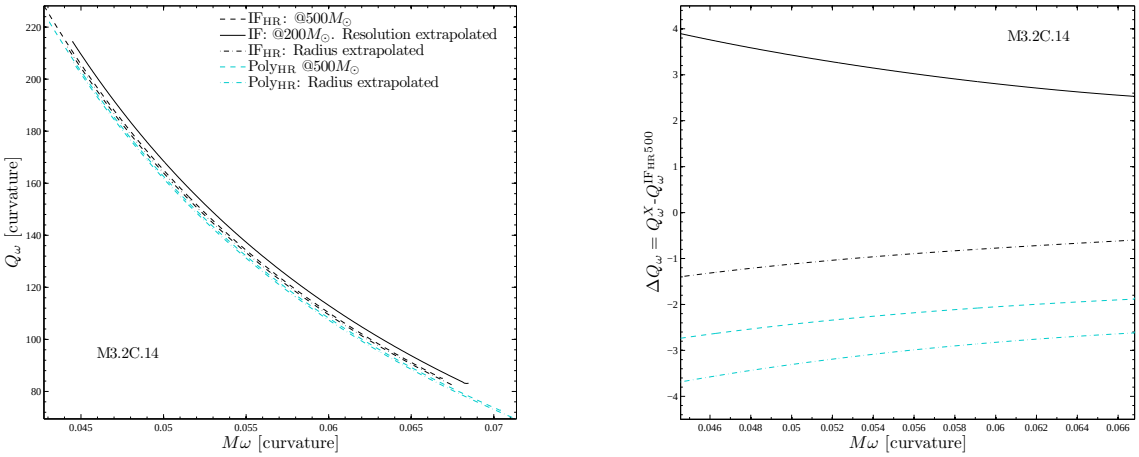

FIG. 7. Left panel: span of Q_ω's due to the various approximations to the curvature waveforms from model `M3.2C.14`. Right panel: the corresponding differences $\Delta Q_\omega = Q^X_\omega - Q^{\rm IF_{HR}500}_\omega$ between the various curves and the fiducial one obtained from the phase computed at the highest resolution and extracted at $500\,M_\odot$.

TABLE III. Uncertainty estimates on the $r\psi_4^{22}$ phase of the IF$_{\rm HR}$500 fiducial simulations obtained from integration of the differences between Q_ω's. From left to right the columns report: the model name, the EOS, the coordinate extraction radius, the type of extrapolation that is performed on the waveform, the frequency interval MI_ω where the cleaning procedure is applied, the corresponding time interval I_t, the accumulated phase difference $\Delta\phi_{\psi_4} = \phi^X - \phi^{\rm IF_{HR}500}$ on a *common* frequency interval MI^c_ω, the number of GW cycles on the same frequency interval, and the relative phase difference $\widehat{\Delta\phi_{\psi_4}} = \Delta\phi_{\psi_4}/\phi_{\psi_4}$. We choose the common interval of integration to be $MI^c_\omega = [0.045, 0.067]$ for model `M3.2C.14` and $MI^c_\omega = [0.037, 0.054]$ for model `M2.9C.12`.

Model	EOS	$r_{\rm obs}$ $[M_\odot]$	Extrap.	MI_ω	I_t $[M]$	$\Delta\phi_{\psi_4}$ [rad]	ϕ_{ψ_4} $[2\pi]$	$\widehat{\Delta\phi_{\psi_4}}$ [%]
`M3.2C.14`	IF	500	–	[0.041, 0.068]	[1000, 2290]	–	9.14	–
`M3.2C.14`	IF	500	radius	[0.044, 0.069]	[1000, 2130]	−0.39	8.99	−1.61
`M3.2C.14`	IF	200	resolution	[0.046, 0.072]	[1000, 2145]	1.28	9.34	2.24
`M3.2C.14`	poly	500	–	[0.041, 0.069]	[1000, 2290]	−0.92	9.07	−0.69
`M3.2C.14`	poly	500	radius	[0.044, 0.072]	[1000, 2030]	−1.24	8.94	−2.16
`M2.9C.12`	IF	500	–	[0.036, 0.058]	[1300, 3366]	–	13.02	–
`M2.9C.12`	IF	500	radius	[0.037, 0.054]	[1300, 3070]	−0.18	13.00	−0.2

B. Q_ω analysis

In Sec. IV we have introduced $Q_\omega = \omega^2/\dot\omega$ as a convenient, intrinsic diagnostics to describe the phasing of the waveform. In particular, it allows us to better visualize the influence of tidal effects on the phasing, as well as to compute the dephasing accumulated on a given frequency interval. It is then useful to recast the various time-domain phase uncertainties on the high-resolution waveform extracted at $500\,M_\odot$ discussed above, in terms of Q_ω. In practice, we apply the cleaning procedure on each waveform of Table II so as to obtain four Q_ω curves. These curves are displayed together in the left panel of Fig. 7, while the fifth column of Table III lists the specific frequency intervals I_ω that were selected to apply the cleaning procedure. For a quantitative assessment of the differences between the Q_ω curves, we present in the right panel of Fig. 7 the quantity $\Delta Q^X_\omega(\omega) = Q^X_\omega(\omega) - Q^{\rm IF_{HR}500}_\omega(\omega)$, where the labelling X indicates any curve other than our fiducial one, IF$_{\rm HR}$500. Although the information conveyed by this figure is qualitatively analogous to the time-domain analysis, Fig. 6, it is made here both independent of any phase-alignment procedure and simpler to quantify. First of all, the figure shows that the extrapolations in radius and in resolution act in different directions: the first one pushes the curve down (i.e., less GW cycles accumulated on a given frequency interval, tidal effects look stronger),

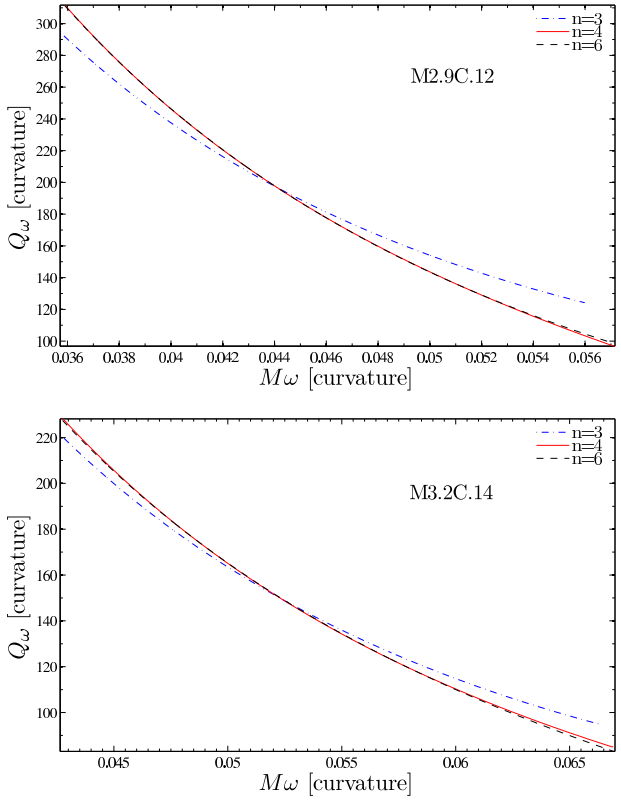

FIG. 8. Sensitivity of Q_ω to the phase model used in the fitting procedure. Note that the $n = 4$ and $n = 6$ curves are barely distinguishable on the plot. See text for details.

while the second one pushes the curve up (i.e., more GW cycles accumulated and tidal effects look weaker). This result is qualitatively compatible with the corresponding $\Delta\phi$ curves in Fig. 6, whose slopes have opposite signs. In addition, by integrating in frequency the ΔQ_ω curves on the *common* frequency interval $MI^c_\omega = [0.045, 0.067]$ one obtains an estimate of an actual accumulated phase error that can be compared to our previous time-domain results (i.e., Fig. 6). The result of this integration is given in the seventh column of Table III. Note that the $\Delta\phi_{\psi_4}$ computed in this way is typically significantly larger than what was estimated above in the time domain. For instance, regarding the comparison with the resolution extrapolated waveform, the Q_ω-based procedure indicates a phase difference of about 1.3 rad over I^c_ω; by contrast, inspecting Fig. 6, where the vertical (red) dashed line corresponds to I^c_ω in the time-domain, we read from the plot an accumulated phase difference on this interval of about 0.8 rad, i.e., about 40% smaller. Similar results hold for the other phase comparisons. This increase in the estimated phase errors is probably due to the additional uncertainty brought by the necessity to use a phase-cleaning procedure to compute each $Q^X_\omega(\omega)$ (see below). This is the price we have to pay to be able to have the convenience of an *intrinsic* diagnostic of the phase evolution.

A separate discussion is needed when comparing isentropic and non-isentropic Q_ω curves. Figure 7 indicates that the curve corresponding to the ideal-fluid EOS lies above the polytropic one, and this indicates that the tidal interaction appears *weaker* in the former case than the latter (because the curve referring to the ideal-fluid is closer to the point-mass curve than the polytropic curve, see below). This effect was already discussed in Ref. [2] and is likely due to the small shocks that are formed by the interaction between the outer layer of the stars and the external atmosphere. The polytropic EOS should yield a priori a more accurate evolution during the inspiral, when the stars are far apart, but should become progressively inaccurate and inconsistent when the two stars become closer and closer, with mass shedding and the formation of actual shocks that are not simply due to the weak interaction with the atmosphere. For this reason we will not use the isentropic Q_ω's as a lower bound in our analysis, but we will focus only on non-isentropic evolutions, though keeping in mind that there is a further source of error on them.

A natural question that comes at this stage is: what is the uncertainty on the determination of the $Q_\omega(\omega)$ function that is due to the phase-cleaning (i.e., phase-fitting) procedure? A first way of addressing this issue is to measure the impact that changing our fiducial fitting function Eq. (28) has on $Q_\omega(\omega)$. Focussing, for both models, only on our basic $\mathrm{IF_{HR}}500$ data, we computed the cleaned frequency using, besides our fiducial fitting polynomial of order $n = 4$ (see Eq. (28)), either a lower-order polynomial truncated at $n = 3$ or a higher-order one, extended up to $n = 6$.[9] The results of these computations are displayed in Fig. 8 for model `M2.9C.12` (top panel) and `M3.2C.14` (bottom). The results are qualitatively analogous in the two cases. First, we see that the low polynomial order $n = 3$ is clearly too small, and fails to capture (when comparing it to the PN or EOB curves, which are accurate on the low-frequency side) the low-frequency behavior of $Q_\omega(\omega)$. By contrast, the fact that the $n = 6$ curve is barely distinguishable (on the scale of the figure) from the $n = 4$ one is an indication of a sort of "convergence" of our fitting procedure as the number of x^n powers is increased. We can therefore use the *difference* between $Q^{n=6}_\omega(\omega)$ and $Q^{n=4}_\omega(\omega)$ as an estimate of the uncertainty $\delta Q_\omega(\omega)$ entailed by the cleaning procedure. Computing this difference, we find that it remains of order unity all over the fitting frequency interval I_ω. In conclusion, we estimate the uncertainty associated with the choice of the order of the fitting polynomial to be $\delta Q_\omega \approx \pm 0.5$. Note that this error is rather small compared to the various numerical errors on $Q_\omega(\omega)$ displayed in Fig. 7, but it is only a lower bound on the uncertainty

[9] Note that $n = 5$ is not meaningful as the corresponding p_5 term is exactly degenerate with ϕ_0. Furthermore, the use of $x^5 \ln x$ does not help, as the corresponding term is nearly degenerate with ϕ_0.

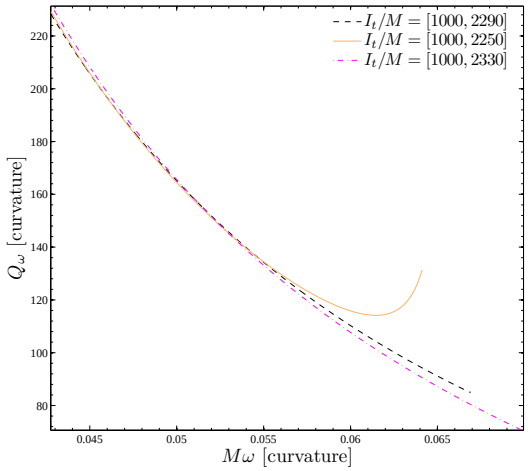

FIG. 9. Sensitivity of Q_ω to the choice of the fitting time-interval I_t for `M3.2C.14`. Our preferred cleaning time-interval $I_t/M = [1000, 2290]$ (central dashed-line) is compared to $I_t/M = [1000, 2250]$ (solid-line) and $I_t/M = [1000, 2330]$ (dash-dotted line). See text for details.

level $\delta^{\rm clean}Q_\omega$ linked to the cleaning procedure.

In particular, another relevant source of uncertainty on Q_ω is the choice of the fitting time interval I_t. In Appendix B we explicitly discuss some rules of thumb that we follow to select I_t such that the cleaning procedure is reliable and robust. To complete the discussion of Appendix B, we investigate (for model `M3.2C.14`) the modifications in Q_ω brought by changes in the choice of I_t. More precisely, we modified the right-end point t_2 of our preferred cleaning time interval $I_t/M \equiv [t_1, t_2] = [1000, 2290]$ (see Table III) by ± 40 (with fixed polynomial order $n = 4$). The three Q_ω curves corresponding to $t_2 = \{2250, 2290, 2330\}$ are displayed in Fig. 9. When comparing the cases $t_2 = \{2250, 2290\}$, we find that the absolute value of the difference in Q_ω stays ≤ 1 all over the time-interval $I_t/M = [1000, 1951]$ (corresponding to a frequency interval $MI_\omega = [0.041, 0.056]$), but then grows up to values of order 30 near $t_2 = 2250$. On the other hand, when comparing the cases $t_2 = \{2290, 2330\}$ we find that the absolute value of the difference in Q_ω stays of order 3 all over I_t. This further analysis suggests that the cleaning procedure allows us to determine Q_ω within an uncertainty level $\delta^{\rm clean}Q_\omega \approx 1$ during most of the inspiral, with a possible increased uncertainty level ≈ 3 near the end of the inspiral. Note that these levels are significantly smaller than the changes in the analytical Q_ω's associated to a variation of the NNLO parameter $\bar{\alpha}_2$ between 0 and 100 (see next Section).

VI. COMPARISON OF ANALYTICAL AND NUMERICAL-RELATIVITY RESULTS

A. Characterizing tidal effects from NR simulations

Before proceeding with the NR/AR comparison it is useful to discuss a procedure by means of which it is possible to effectively subtract the tidal interaction from the NR Q_ω curves obtained so far. This procedure will then allow us to obtain a phase diagnostic Q^0_ω that, within some approximation, represents a non-tidally interacting binary, namely a binary of two point-particles. As pointed out in Ref. [21], the binding energy of a binary system $E_b(\Omega)$ is approximately linear in κ^T_2 and it is therefore possible to subtract the tidal effects by combining different sets of binding-energy curves coming out of NR calculations. In particular, Ref. [21] computed several "tidal-free" binding energy curves (one curve for each combination of two different data sets) that were compared with the corresponding point-mass curve computed within the EOB approach or within non-resummed PN theory. This procedure allowed for both the identification (and thus subtraction) of systematic uncertainties in the NR data and the discovery of higher-order tidal amplification effects.

Here we will generalize the approach introduced in Ref. [21] to the Q_ω curve. In particular we assume that the function $Q_\omega(\omega)$ is approximately linear in the (leading) tidal parameter κ^T_2, at least during part of the inspiral, say up to some maximum frequency $\omega_{\rm max}$ (we will use $\omega_{\rm max} \approx 0.07$). As a result of this assumption, we can approximately write $Q_\omega(\omega)$, for each binary, as

$$Q_\omega(\omega; I) = Q^0_\omega(\omega) + (\kappa^T_2)_I\, Q^2_\omega(\omega) + \mathcal{O}\left((\kappa^T_2)^2\right) , \quad (35)$$

where I is an index labelling some binary system. As a result, given the Q_ω diagnostics of two different binaries with labels (I, J), we can estimate the two separate functions $Q^0_\omega(\omega)$ and $Q^2_\omega(\omega)$ as

$$Q^0_\omega(\omega) = \frac{(\kappa^T_2)_I Q_\omega(\omega; J) - (\kappa^T_2)_J Q_\omega(\omega; I)}{(\kappa^T_2)_I - (\kappa^T_2)_J} , \quad (36)$$

$$Q^2_\omega(\omega) = \frac{Q_\omega(\omega; I) - Q_\omega(\omega; J)}{(\kappa^T_2)_I - (\kappa^T_2)_J} . \quad (37)$$

From the decomposition (35), we see that, by definition, the function Q^0_ω denotes the Q_ω diagnostic of two non-tidally interacting NSs, namely of two point-like (relativistic) masses (and also two BHs [18, 19]). Hence, the function $Q^2_\omega(\omega)$ is seen to represent, within the present approximation, the effect of the tidal interaction on the Q_ω function. The calculation of both functions contains therefore important information about the analytical representation of tidally-interacting binary systems. In the following we will only discuss the computation of the tidal-free part $Q^0_\omega(\omega)$, leaving a discussion of the properties of $Q^2_\omega(\omega)$ to a future work.

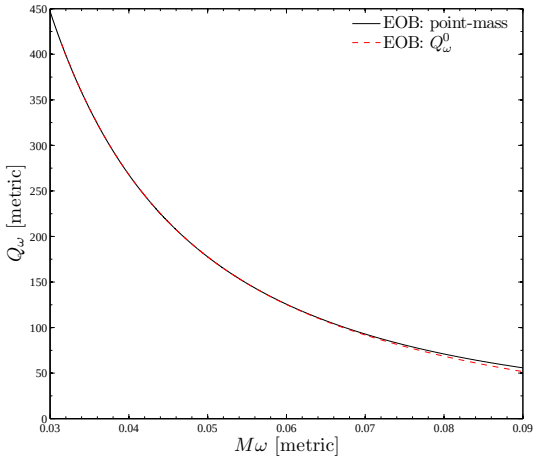

FIG. 10. Subtraction of tidal effects: shown as a solid line is the point-mass EOB curve, while shown as a dashed line is the Q^0_ω curve obtained by inserting in Eq. (36) the tidally-modified EOB Q_ω curves shown in Fig. 3.

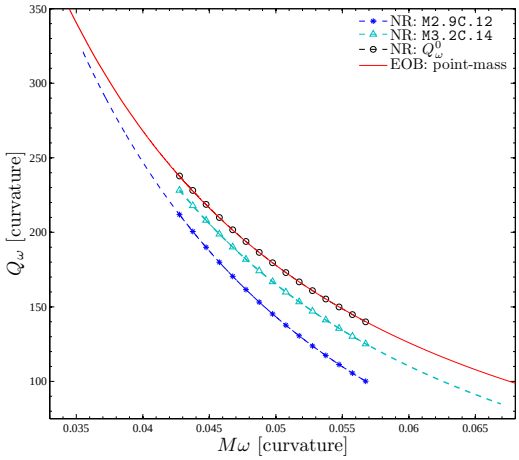

FIG. 11. Subtraction of tidal effects from numerical relativity (curvature) Q_ω curves according to Eq. (36). Note the excellent agreement with the point-mass EOB curve in the frequency window where M2.9C.12 and M3.2C.14 data overlap. The relative EOB-NR phase difference accumulated over this overlap interval is $\Delta\phi^{\rm EOBNR}_{\psi_4} = -0.03$ rad.

This subtraction procedure for computing $Q^0_\omega(\omega)$ can be first tested by using the EOB metric waveforms computed from binaries with compactnesses $\mathcal{C} = 0.12$ and $\mathcal{C} = 0.14$. The result of the subtraction is displayed in Fig. 10, where we compare the point-mass (i.e., BBH) EOB Q_ω curve (solid line) to the Q^0_ω curve (dashed line), obtained by inserting in Eq. (36) the $\mathcal{C} = 0.12$ and $\mathcal{C} = 0.14$ data of Fig. 3. The fact that the curves are barely distinguishable up to $M\omega = 0.07$ (where the difference is $\Delta Q_\omega \approx 1$) gives us confidence that the procedure will be effective also with actual NR data. This will indeed be shown in the next Section.

B. Inspiral: subtracting tidal effects from NR data

We start our NR/AR comparison by computing the Q^0_ω function as defined by Eq. (36) from NR data using our two models M2.9C.12 and M3.2C.14 as the binaries labelled Ig and J in that equation. For all the comparisons carried out here we have limited ourselves to using the curvature waveforms, although similar results can be obtained from the corresponding metric waveforms.

The results are shown in Fig. 11, which reports four different Q_ω curves: the two tidally-modified NR Q_ω curves for the binaries M2.9C.12 and M3.2C.14 (with the asterisks and triangles highlighting a sample of the data on the common frequency window), the subtracted NR Q^0_ω curve (with empty circles), and the point-mass-EOB Q_ω (as a solid line). This figure illustrates at once several of the main results of this paper. First of all, it highlights the excellent agreement between the cleaned NR Q^0_ω and the analytical EOB one (cf. the red solid curve and the empty circles). This gives evidence both for the validity of the EOB description and for the robustness of our cleaning procedure. When we compute the relative phase difference over the common frequency interval $[0.042, 0.055]$, we obtain the remarkably small value of $\Delta\phi^{\rm EOBNR}_{\psi_4} \equiv \phi^{\rm EOB} - \phi^{\rm NR} = -0.03$ rad, which translates into a relative difference $\Delta\phi^{\rm EOBNR}_{\psi_4}/\phi^{\rm EOBNR}_{\psi_4} = 0.02\%$ [10]. Second, it confirms, independently of our EOB-based check (cf. Fig. 10), that the NR tidal effects are approximately linear in κ^T_2 at least in the early part[11] of the waveform, and thus that they can be efficiently subtracted. Third, it illustrates the fact that the tidal interaction between the two objects is important already in the early-inspiral part of the waveform, since both the M2.9C.12 and M3.2C.14 curves are significantly displaced (by $\Delta Q_\omega \sim 10$) with respect to the point-mass one. Fourth, such a good agreement with the point-mass EOB analytical model (which was tuned so as to accurately reproduce the equal-mass BBHs) yields an independent check of the consistency and accuracy of our numerical simulations. Finally, we note that in Ref. [21] the

[10] To cross-check the consistency of both the recovery procedure of h_{22} from ψ^{22}_4 and the cleaning of the phase, we carried out the same calculation also for the metric waveforms, finding a difference $\Delta\phi^{\rm EOBNR}_h = +0.05$ rad, which is consistent with the estimated error-bar $\Delta\phi = \pm 0.02$ rad on the EOBNR point-mass waveform during inspiral [27].

[11] In the following, we will refer to the frequency domain $M\omega \lesssim 0.06$ as the "early-inspiral". Note that for a fiducial $1.4\,M_\odot - 1.4\,M_\odot$ system $M\omega = 0.06$ corresponds to $f_{\rm GW} = 690$ Hz. Note also that in the case, for instance, of our $\mathcal{C} = 0.14$ system the frequency $M\omega = 0.06$ is reached at time $t \simeq 2000M$, i.e., only about 5 GW cycles before merger.

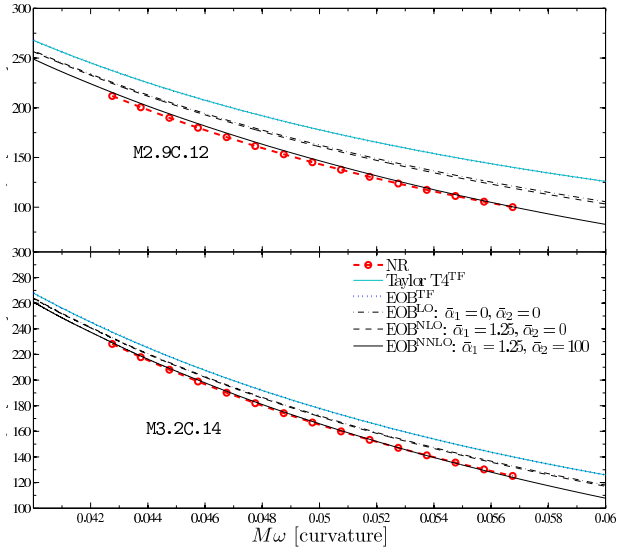

FIG. 12. Comparison of the EOB Q_ω curves for different choices of the effective tidal amplification factor $\hat{A}_\ell^{\rm tidal}(u) = 1 + \bar{\alpha}_1 u + \bar{\alpha}_2 u^2$, with the corresponding NR ones (dashed lines with open circles) for the two binaries considered. The dotted line corresponds to the "tidal free" (or "point-mass") EOB, namely, when ignoring tidal effects. The figure also includes the tidal-free Taylor-T4 model. The good visual agreement between the analytic and the numerical curves for $\bar{\alpha}_2 = 100$ provides evidence of the need for large NNLO tidal corrections. The corresponding phase differences $\Delta\phi_{\psi_4} = \phi^{\rm EOB} - \phi^{\rm NR}$ are listed in Table IV.

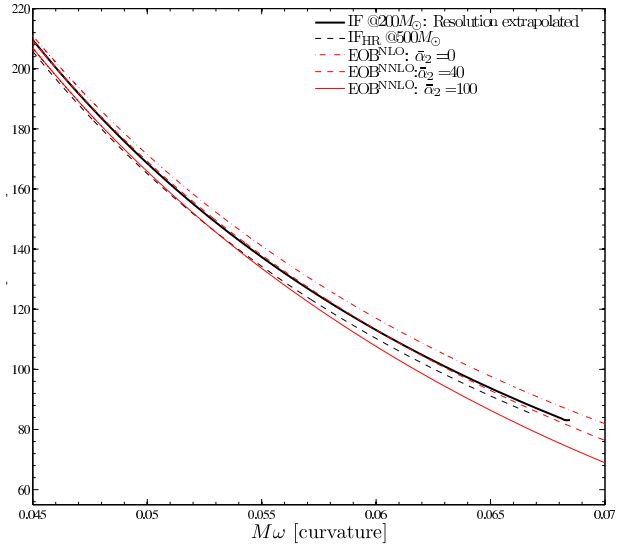

FIG. 13. Magnitude of NNLO tidal effects: span of EOB Q_ω curves (red) with varying $\bar{\alpha}_2$ so as to be compatible with the various (numerical) Q_ω curves (black).

procedure of subtraction, applied there to the NR binding energy, was giving a curve slightly displaced with respect to the point-mass EOB (or PN) curve. This displacement was interpreted as evidence of systematic errors in the NR simulation and prompted the introduction of a "correcting" procedure, which however is not necessary for the present NR data.

C. Early inspiral: evidence for large NNLO tidal effects

We continue our analysis by focussing on the influence of LO tidal effects on the early-frequency part of the Q_ω curves. We already know from Fig. 11 that tidal effects are important in such early-frequency part of the simulations, since we found a significant difference (of order 10) between the point-mass curve and the NR ones. Can these differences be accounted just by the LO tidal effects? Figure 12 shows quite clearly that this is not the case and that the LO description *is not sufficient* to match the corresponding NR curves (dashed line with open circles). Note that this is the case for both the `M2.9C.12` (upper panel) and the `M3.2C.14` binaries (lower panel). The difference with NR data (on the frequency interval $[0.043, 0.057]$ where the data of `M2.9C.12` and `M3.2C.14` overlap) is quantified in the first line of Table IV and is rather large, namely several radians.

We next turn to analyzing the effect of NLO and NNLO tidal interactions. Here, we will regroup under the label of NLO both 1PN and 1.5PN effects. As seen in Fig. 12, the inclusion of the NLO tidal effects ($\bar{\alpha}_1 = 1.25$ [21], 1PN tidal-radiation effects [29], and 1.5PN tail effects) has only a barely noticeable effect on the Q_ω curve. This clearly indicates the need for large NNLO (2PN and higher) tidal effects, which we chose to parameterize by means of the effective parameter $\bar{\alpha}_2 \equiv \bar{\alpha}_2^{(\ell)}$ introduced in Eq. (14). We then found that choosing $\bar{\alpha}_2 = 100$ yields a good match between the NR and EOB Q_ω curves (solid line, EOB$^{\rm NNLO}$), especially for the `M3.2C.14` model, for which the analytical curve is on top of the NR data. See also Table IV for the corresponding phase differences. The Table also indicates that if we use $\bar{\alpha}_2 = 130$, as we did in Ref. [1], the accumulated dephasing on the common frequency interval $[0.043, 0.057]$ is further reduced to a fraction of a radian for both models. Note that the implementation of the EOB waveform and radiation reaction that we use here is slightly different with respect to the one of [1], which was based on Ref. [21] and thus did not incorporate the waveform 1PN corrections [29] nor the tail effects. This explains why we were quoting different phase differences ($\Delta_I \phi^{\rm EOBNR} \approx 0.1$ rad) over the same interval when referring to $\bar{\alpha}_2 = 130$ in [1]. However, we prefer here the smaller value $\bar{\alpha}_2 = 100$ because the corresponding Q_ω curve is, on average, closer to the NR one on the *larger frequency interval* $[0.041, 0.068]$ on which we succeeded to clean the NR phase.

It is important to recall that various numerical errors affect the computation of the NR Q_ω curves, and thereby affect the quantitative determination of the ef-

fective NNLO parameter $\bar{\alpha}_2$. For example, we have seen that the resolution extrapolation (which seemed to be the dominant source of uncertainty) has the practical effect of pushing the numerical Q_ω curve *upwards*. This suggests that the value $\bar{\alpha}_2 \simeq 100$ obtained from using finite-resolution NR data is probably too large. To have a rough idea of the error range on $\bar{\alpha}_2$, we compare in Fig. 13 various NR and EOB curves. More precisely, this figure shows two numerical Q_ω black curves: a solid one, derived from our fiducial highest-resolution and largest-extraction-radius $\mathrm{IF}_{\mathrm{HR}}500$, and a dashed one, derived from the resolution-extrapolated NR data. Also reported in Fig. 13 are three analytical curves (red lines): namely the EOB predictions for the three values $\bar{\alpha}_2 = 0, 40, 100$, respectively. Clearly, the resolution-extrapolated Q_ω curve is close to the analytical curve corresponding to the value $\bar{\alpha}_2 \simeq 40$, which is more than twice smaller than the value $\bar{\alpha}_2 \simeq 100$ suggested by our fiducial, highest-resolution NR data. It is interesting to note that the value $\bar{\alpha}_2 \simeq 40$ agrees with the preferred value of $\bar{\alpha}_2$ (when using $\bar{\alpha}_1 = 1.25$) found in [21], the work that pinpointed the first evidence for the need of large NNLO effects. Let us also note that, independently of the precise value of $\bar{\alpha}_2$, Fig. 13 clearly shows the need for large NNLO effects, namely $\bar{\alpha}_2 \gtrsim 40$.

Let us also recall that the other sources of numerical error act in various directions. For instance, non-isentropic effects actually act so as to effectively reduce the magnitude of the tidal interaction[12], while the extrapolation to infinite extraction radius acts in the opposite direction, namely effectively increasing the magnitude of the tidal interaction.

In view of our incomplete knowledge of all the sources of error intervening in our NR waveforms, we can only conclude that $\bar{\alpha}_2$ probably lies in the range $40 \lesssim \bar{\alpha}_2 \lesssim 130$, with the understanding that the lower values ($\bar{\alpha}_2 \simeq 40$) are preferred because of the expected importance of the truncation error in the numerical simulations. More numerical simulations with a more detailed estimate of the numerical error budget will be needed in the future to reduce this error range on $\bar{\alpha}_2$.

Let us conclude this Section by briefly discussing the comparison between the NR Q_ω diagnostics with those obtained using several versions of the Taylor-T4 approximant. More precisely, Fig. 14 displays the following Q_ω curves: the tidal-free T4 model (T_4^{TF}, dotted line), the LO Taylor-T4 model (dashed-line), the NLO (i.e., 1PN) one (dash-dotted line), and finally the effective NNLO one (solid line), as introduced in Sec. III C above. Let us recall that the NNLO model contains an effective 2PN parameter, called a_2^{T4}, which is a rough T4 analog of the NNLO EOB parameter $\bar{\alpha}_2$ and which enters the T4 tidal amplification factor Eq. (23). Similarly to the EOB case, one finds that a suitably large value of the effective 2PN tidal parameter a_2^{T4} can provide curves that are close to the numerical ones. The integrated dephasings $\phi^{\mathrm{T4}} - \phi^{\mathrm{EOB}}$ corresponding to Fig. 14 are listed in Table IV.

TABLE IV. Measuring the phase difference between NR (curvature) waveforms and analytic ones (from both EOB and Taylor T4 models). The phase differences are computed on the frequency interval $[0.043, 0.057]$ common to both Q_ω numerical curves. From left to right, the columns report: the type of analytical model, the magnitude of the effective parameters yielding NNLO tidal corrections; and the dephasings $\Delta\phi_{\psi_4} = \phi^X - \phi^{\mathrm{NR}}$ (with X being either EOB or T4) for both `M2.9C.12` and `M3.2C.14` data obtained by direct integration of the corresponding Q_ω's of Figs. 12 and 14 over the common interval $[0.043, 0.057]$.

Model	NNLO parameters	$\Delta\phi_{\psi_4}^{\mathtt{M2.9C.12}}$ [rad]	$\Delta\phi_{\psi_4}^{\mathtt{M3.2C.14}}$ [rad]
$\mathrm{EOB}^{\mathrm{LO}}$	$\bar{\alpha}_2 = 0$	5.04	1.74
$\mathrm{EOB}^{\mathrm{NLO}}$	$\bar{\alpha}_2 = 0$	4.62	1.58
$\mathrm{EOB}^{\mathrm{NNLO}}$	$\bar{\alpha}_2 = 100$	1.06	0.17
$\mathrm{EOB}^{\mathrm{NNLO}}$	$\bar{\alpha}_2 = 130$	0.056	−0.25
$\mathrm{T4}^{\mathrm{LO}}$	$a_2^{\mathrm{T4}} = 0$	6.64	2.33
$\mathrm{T4}^{\mathrm{NLO}}$	$a_2^{\mathrm{T4}} = 0$	6.42	2.25
$\mathrm{T4}^{\mathrm{NNLO}}$	$a_2^{\mathrm{T4}} = 350$	1.53	0.15

A few comments are worth making on the comparison between the EOB and T4 results. Let us first recall that, in the BBH case, it has been shown that the EOB description is definitely more accurate than the Taylor-T4 one, especially when considering unequal mass ratios [46] or spin effects [61]. However, as we are considering here an equal-mass case and frequencies that are smaller (when considering the dimensionless frequencies $M\omega$) than in the BBH case, the tidal-free T4 phasing is quite close to the EOB one (see Fig. 12). Concerning tidal-extended models, we see that both EOB and T4 approximations highlight the need for large higher-order tidal-amplification factors. When choosing one such amplification factor for both BNS systems (say $\bar{\alpha}_2 = 100$ for EOB and $a_2^{\mathrm{T4}} = 350$ for T4), a close look at the comparison of the corresponding Q_ω curves suggests that the EOB-predicted curves are somewhat closer than the T4-predicted one to the NR curves. However, this, by itself, would only be a weak indication that EOB gives a better representation of our fiducial NR data, especially in view of the large uncertainties discussed above on the actual value of the $Q_\omega(\omega)$ functions. On the other hand, we consider that the need of a much larger tidal-amplification factor in the T4 case is an indication that the analytical modelling of (LO, NLO and NNLO) tidal effects within the EOB-resummed framework might be more robust

[12] Indeed the non-isentropic Q_ω curve lies above the isentropic one. This is certainly a source of error during the early-inspiral, where the isentropic description is a priori more accurate but some energy is channelled by shocks due to the interaction with the atmosphere.

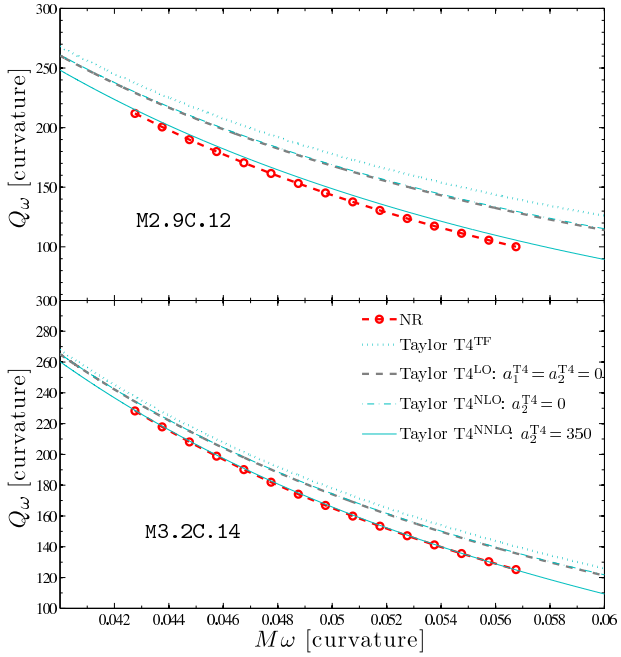

FIG. 14. Comparison of the Taylor-T4 Q_ω curves for different choices of the effective tidal amplification factor $\hat{a}^{\rm tidal}(u) = 1 + a_1^{\rm T4}x + a_2^{\rm T4}x^2$, with the corresponding NR ones (dashed lines with open circles) for the two binaries considered. The dotted line corresponds to the "tidal free" (or "point-mass") T4, namely, when ignoring tidal effects. Note that the value $a_2^{\rm T4} = 350$ of the dimensionless NNLO effective tidal correction parameter that best matches the (`M3.2C.14`) NR data is considerably larger than in the EOB case. The corresponding phase differences $\Delta\phi_{\psi_4} = \phi^{\rm T4} - \phi^{\rm NR}$ are listed in Table IV.

than the corresponding one based on Taylor-expanded approximants. Indeed, in both cases the parametrization of NNLO effects involves multiplying tidal effects by a factor having a similar structure: $\hat{A}_\ell^{\rm tidal(EOB)}(u) = 1 + \bar{\alpha}_1^{(\ell)}u + \bar{\alpha}_2^{(\ell)}u^2$ versus $\hat{a}_{\rm T4}^{\rm tidal}(u) = 1 + a_1^{\rm T4}x + a_2^{\rm T4}x^2$. In addition, the quantities u and x are numerically close to each other (both being close to $(M\omega/2)^{2/3} \sim v^2/c^2$). At the end of the inspiral, $M\omega$ reaches numerical values of order 0.1 (i.e., 1154 Hz for a fiducial BNS system), corresponding to $u \simeq x \simeq 0.136$. For such a value one sees that the EOB amplification factor (with $\bar{\alpha}_2 = 100$) remains relatively moderate[13], namely $\hat{A}_\ell^{\rm tidal(EOB)}(u) = 1 + 1.25u + 100u^2 \simeq 1 + 0.17 + 1.85 \simeq 3$, while the T4 one (with $a_2^{\rm T4} = 350$) is suspiciously large, and is completely dominated by the 2PN contribution, namely $\hat{a}_{\rm T4}^{\rm tidal}(u) = 1 + 1.19x + 350x^2 = 1 + 0.16 + 6.47 = 7.63$. Another way to phrase this is to notice that the large T4 value $a_2^{\rm T4} = 350$ is such that the 2PN contribution $a_2^{\rm T4}x^2$ starts dominating the LO term at $x = 1/\sqrt{350} \simeq 1/18.7$, i.e., at large separations $r \simeq 18.7M$ corresponding to rather low frequencies $M\omega = 2x^{3/2} = 0.025$, i.e., 285 Hz for a fiducial BNS system. Furthermore, such a large value for $a_2^{\rm T4}$ works well for binary `M3.2C.14`, but less well for binary `M2.9C.12`.

Clearly, in view of the large current uncertainties on the Q_ω NR curve, more work is needed to confirm this provisional conclusion. In particular, more accurate NR simulations, encompassing more compactnesses and different mass ratios will be needed to assess the relative merits of the EOB versus the Taylor-T4 description of tidally interacting BNS systems.

D. EOB/NR phasing

So far our NR/AR comparison based on the function $Q_\omega(\omega)$ has been limited to a frequency interval which did not cover the last octave of frequency evolution, even if, when viewed in the time domain, this interval covered most of the cycles of the inspiral. In this section we finally focus on a phasing comparison in the time domain which covers *the full inspiral and plunge phase*, up to the merger of the two NSs. Our strategy here will not be to explore from scratch a good range of values of the tidal NNLO parameter $\bar{\alpha}_2$ values, but instead to use the value $\bar{\alpha}_2 = 100$ suggested by our previous $Q_\omega(\omega)$-analysis, and to explore to what extent it succeeds in providing a waveform which agrees with our fiducial (highest-resolution) NR waveform over the full inspiral. Anticipating our conclusion, we will find that the EOB waveform with $\bar{\alpha}_2 = 100$ does closely agree (both in phase and modulus) with the NR waveform essentially up to the merger.

This is shown in Fig. 15, which compares the (real part of the) EOB and NR metric rh_{22} waveforms for the case including NNLO effects with $\bar{\alpha}_2 = 100$. The left panels refer to the `M2.9C.12` binary, while the right panels refer to the `M3.2C.14` one. The top panels show the real parts of both the EOB and NR h_{22} waveforms (divided by the symmetric mass ratio ν); the middle panels display instead the corresponding phase differences $\Delta\phi^{\rm EOBNR}(t) = \phi^{\rm EOB}(t) - \phi^{\rm NR}(t)$, for both metric (solid line) and curvature (dashed line) waveforms, for completeness; the bottom panels compare the EOB (dashed line) and NR (solid line) instantaneous GW frequency. The least-squares phase alignment has been performed on the time interval $[t_L, t_R]/M = [250, 3300]$ for the `M2.9C.12` binary and $[t_L, t_R]/M = [250, 2250]$ for the `M3.2C.14` one.

The two vertical lines (dot-dashed and dashed) indicate the "end of the inspiral phase", as defined either within the EOB analytical framework (dot-dashed line) or by using NR information (dashed line). Note that we call here simply "inspiral" what was called "insplunge" in previous EOB studies, namely the union of the inspiral and (when it is reached before merger) of the plunge. More precisely, the dashed line indicates the NR-defined "merger", i.e., the time (computed from the NR data)

[13] For $\bar{\alpha}_2 = 40$, this amplification factor becomes $\hat{A}_\ell^{\rm tidal(EOB)}(u) = 1 + 1.25u + 40u^2 \simeq 1 + 0.17 + 0.74 \simeq 1.91$

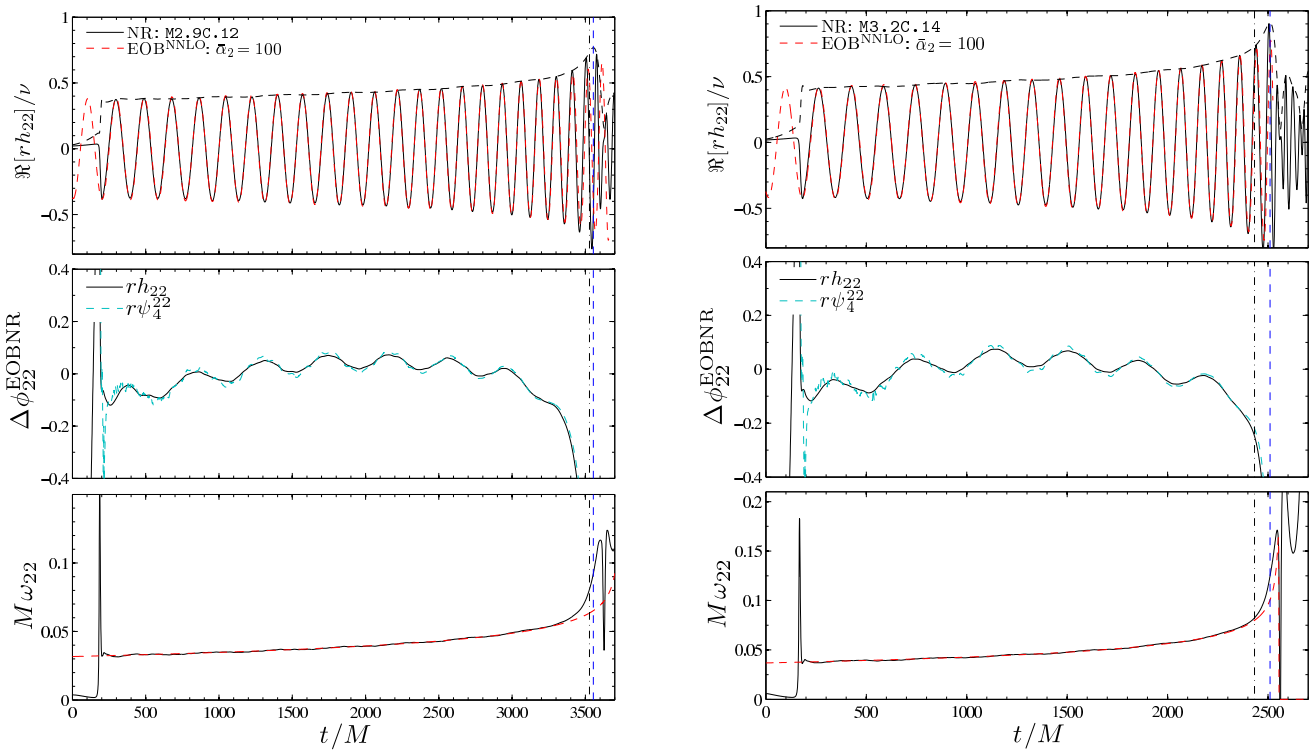

FIG. 15. Comparison between EOB and NR phasing for the M2.9C.12 (left panels) and M3.2C.14 (right panels) binaries. The top panels show the real parts of the EOB and NR h_{22} waveforms, the middle panels display the corresponding phase differences $\Delta\phi^{\rm EOBNR} = \phi^{\rm EOB} - \phi^{\rm NR}$, both metric (solid line) and curvature (dashed line) waveforms, the bottom panels compare the EOB (dashed line) and NR (solid line) instantaneous GW frequency. The NNLO corrections to the radial potential are carried out with the parameter $\bar{\alpha}_2 = 100$. Note the agreement reached with the numerical waveform almost up to the time of the merger as defined in terms of the maximum of the GW amplitude (vertical dashed line) or of the contact position (dot-dashed line; see the text for details).

at which the modulus of the metric waveform reaches its first maximum. On the other hand, the vertical dash-dotted line indicates the EOB-defined "contact" between the two NSs[14]. Such a formal contact moment was introduced in Eqs. (72) and (77) of Ref. [21], by a condition expressing that the EOB radial separation R becomes equal to the sum of the tidally deformed radii of the two NSs, namely

$$R^{\rm contact} = (1 + h_2^A\, \epsilon_A(R^{\rm contact}))\, R_A + \{\, _A \;\leftrightarrow\; _B\}\,, \quad (38)$$

where $\epsilon_A(R) = M_B R_A^3/(R^3 M_A)$ is the dimensionless parameter controlling the (LO) strength of the tidal deformation of the NS labeled A by its companion B and where $h_2^{A,B}$ is the shape Love number [18, 62]. A recent study of the tidally induced shape deformation of BHs [62] has shown that the BH shape Love number h_2 was a function of the separation r, which increased as r decreased (and u increased). This behavior is similar to the behavior of the (effective) quadrupole Love number $k_2^{\rm eff}(u) = k_2(1 + \alpha_1^{(2)} u + \alpha_2^{(2)} u^2)$, where both $\alpha_1^{(2)}$ and $\alpha_2^{(2)}$ were found to be positive [21]. One would need a special study devoted to the comparison of the EOB-predicted NS shape deformation to NR data to investigate in detail the u dependence of the analogous $h_2^{\rm eff}(u) = h_2(1 + \gamma_1^{(2)} u + \gamma_2^{(2)} u^2)$. Leaving to future work such a study, we will here replace the u-dependent effective shape Love number $h_2^{\rm eff}(u)$ by a constant, chosen such that the EOB-predicted contact happens *before* the NR-defined merger for the two BNS systems we consider. We found that $h_2^{\rm eff} = 3$ works, and this is the value we will use to replace h_2^A and h_2^B in the contact condition written above[15]. An important point to note is that our (EOB-based) analytical definition of contact allows one to analytically predict a complete inspiral waveform, in-

[14] Note that the styles of the corresponding merger and contact vertical lines as depicted in the two panels of Fig. 2 of Ref. [1] are inverted with respect to the text there. See the arXiv version for the correct figures.

[15] A similar approach was taken in [1, 18], with a less conservative value $h_2^{\rm eff} = 1$. Let us recall that the computation of the infinite-separation shape Love number $h_2 = h_2^{\rm eff}(u = 0)$ of NSs gives values of order unity [18].

cluding its termination just before merger.

Figure 15 shows that the agreement in the time domain between the analytic EOB description and the fully numerical one is extremely good essentially up to the merger. More precisely, the match between the two descriptions is excellent both in modulus and in phase, with a dephasing of order $\Delta\phi = \pm 0.1$ rad during most of the long inspiral phase. It is only during the last $100M$ before contact that the dephasing grows significantly. One should note that this excellent EOB/NR agreement holds for *both* binaries `M3.2C.14` and `M2.9C.12`, and has been obtained by tuning a *single* tidal-amplification parameter.

Clearly the results presented here give only a first cut at these issues. More NR/AR comparisons are needed to confirm our findings and to determine the most effective value of $\bar{\alpha}_2$. With sufficiently accurate NR data one can hope to determine not only the effective tidal-amplification factor $\hat{A}_\ell^{\rm tidal}(u) = 1 + \bar{\alpha}_1 u + \bar{\alpha}_2 u^2$, but also the precise separation-dependence of $\hat{A}_\ell^{\rm tidal}(u)$. This would allow one to extend the EOB description right up to the merger.

VII. CONCLUSIONS

We have presented the first comprehensive NR/AR comparison of the gravitational waveforms emitted during the inspiral of relativistic BNSs as computed via state-of-the-art numerical-relativity simulations and as modelled via state-of-the-art analytical approaches. Overall, the work reported here and our findings can be summarized as follows.

1. We have considered the longest to date numerical simulations of inspiralling and coalescing equal-mass BNSs modeled either with an ideal-fluid or a polytropic EOS. Because tidal effects are most sensitive to the stellar compactness, we have considered two binaries with either a small compactness of $\mathcal{C} = 0.1199$ or with a large compactness of $\mathcal{C} = 0.1396$. The parts of the waveforms relative to the inspiral cover between 20 and 22 cycles and have been studied to isolate possible sources of error, such as non-isentropic evolutions, finite-radii GW extractions, and the use of finite resolutions. For the model with the highest compactness, the first two sources of errors lead to a total error-bar in the GW phase of $\Delta\phi \simeq \pm 0.15$ rad, while the error coming from a finite resolution indicates an accumulated phase error of $\Delta\phi \simeq \pm 0.54$ rad.

2. We have used the function $Q_\omega(\omega) \equiv \omega^2/\dot{\omega}$ as a useful diagnostic of the physics driving the evolution of the GW frequency ω. The calculation of this quantity is however challenging when made from the early-inspiral part of the NR waveforms, as the latter is affected by a series of contaminating errors. We have filtered out these errors by fitting the NR phase evolution $\phi(t)$ with a simple analytical expression that reproduces at lower order the behavior expected from the PN approximation. We have compared the various Q_ω's obtained from different data to estimate the error range entailed by comparing analytical predictions to our highest-resolution, largest-extraction-radius NR data.

3. Using the estimated $Q_\omega(\omega)$ function we have shown that it is possible, at least for frequencies $M\omega \lesssim 0.06$ (i.e., $f_{\rm GW} \lesssim 700$ Hz for a fiducial $1.4\,M_\odot - 1.4\,M_\odot$ BNS system), to *subtract the tidal-effect contribution* from the NR waveforms and consistently match this with the expected EOB model for point particles which has been successfully matched to BBH simulations. The ability to perform this match accurately provides us with an independent validation of the quality of our numerical results as well as with a confirmation that the function $Q_\omega(\omega)$ is approximately linear in the (leading) tidal parameter κ_2^T.

4. The comparison of analytical predictions with NR data shows that tidal effects are significantly amplified by higher-order (NNLO) relativistic corrections even in the early inspiral phase. These NNLO tidal corrections are parameterized within the EOB approach by a unique (effective, 2PN) tidal parameter $\bar{\alpha}_2$. Although the most precise available at the moment, the quality of the NR data is such that we can only constrain the actual value of $\bar{\alpha}_2$ to be in the range $40 \lesssim \bar{\alpha}_2 \lesssim 130$.

5. Once a *single* choice for $\bar{\alpha}_2$ is made, the EOB-predicted waveforms agree (both in phase and in modulus) with the NR ones (for both BNS systems) within their error bar and essentially up to the merger.

6. Finally, we have also compared the NR phasing with the one predicted by a non-resummed Taylor-T4 PN expansion, completed by additional tidal terms. If one uses only the currently known analytic T4 tidal terms, the T4 model dephases (when $\mathcal{C} = 0.12$) by more than 2π rad already at the GW frequency $M\omega = 0.057$, which is about twice smaller than the GW frequency at merger (we recall that $M\omega = 0.057$ corresponds to 658 Hz for a fiducial $1.4\,M_\odot - 1.4\,M_\odot$ system). On the other hand, a good match (for both compactnesses) with the NR phasing is possible if one allows for a T4 analog of the EOB $\bar{\alpha}_2$ parameter, i.e., an (effective) 2PN amplification of tidal effects. The corresponding parameter $a_2^{\rm T4} \simeq 350$ is suspiciously large, works well for binary `M3.2C.14` but less well for binary `M2.9C.12`, and dominates the amplification of tidal effects already at frequencies $M\omega = 0.025$ (corresponding to 285 Hz). This seems to suggest that the EOB-based representation of tidal effects is more reliable than the Taylor-T4 one.

In summary, the work presented here opens new avenues to the important synergy between numerical and analytic descriptions of inspiralling compact-object binaries in general relativity. For the first time we have shown that an analytic modelling is possible also for objects which cannot be treated as point-particles and for which, therefore, tidal effects represent important corrections. Although the results presented here are very encouraging, a number of improvements are needed on both the numerical and the analytical sides. On the numerical side, higher resolutions and better measures of the convergence rates (which are particularly challenging in non-vacuum simulations) are needed to decrease the numerical phase errors to and reach firm conclusions about the tidal contributions to the phasing. On the analytical side, higher-order PN calculations are needed to better determine the form of the NNLO corrections. Both of these goals will be the subject of our future work. Hopefully, progress on both fronts will enable us to determine the crucial tidal-induced dephasing function $\Delta^{\rm tidal}\phi(\omega)$ with an accuracy sufficiently high to extract reliable information on the EOS of matter at nuclear densities [16].

ACKNOWLEDGMENTS

We are grateful to Sebastiano Bernuzzi for discussion throughout the development of this work and to Francesco Pannarale for useful input. The simulations were performed on the Ranger cluster at the Texas Advanced Computing Center through TERAGRID allocation TG-MCA02N014, and on the cluster Damiana of the AEI. This work was supported in part by the DFG Grant SFB/Transregio 7, by "CompStar", a Research Networking Programme of the European Science Foundation, by the JSPS Grant-in-Aid for Scientific Research (19-07803), by the MEXT Grant-in-Aid for Young Scientists (22740163), and by NASA Grant No. NNX09AI75G.

Appendix A: Computing metric waveforms from ψ_4

We discuss here the details of how to accurately derive the metric waveforms $h_{+,\times}$ from the numerically computed curvature waveforms ψ_4. We first recall that the procedure outlined in Ref. [46] consisted essentially of three steps. (i) First one performs the double integration of $\psi_4^{\ell m}$ starting at $t=0$ with the integration constants set to zero; this amounts to defining

$$\dot{h}_0^{\ell m}(t) \equiv \int_0^t dt' \psi_4^{\ell m}(t'), \tag{A1}$$

$$h_0^{\ell m}(t) \equiv \int_0^t dt' \dot{h}_0^{\ell m}(t'). \tag{A2}$$

The provisional metric waveform $h_0^{\ell m}$ differs from the "exact" metric waveform (6) (integrated from past infinity) by a linear function of t, say

$$h_0^{\ell m}(t) = h^{\ell m}(t) + \alpha_{\rm exact} t + \beta_{\rm exact}. \tag{A3}$$

(ii) The second step consists in obtaining an estimate of the two (complex) integration constants $(\alpha_{\rm exact}, \beta_{\rm exact})$ that enter the metric waveform (6) by fitting over the full simulation time interval the $(t \geq 0)$-integrated waveform (A2) to a linear function of t, say $h_0^{\rm lin-fit} = \alpha t + \beta$, where α and β are complex quantities. (iii) The third and final step of the procedure of Ref. [46] consisted in subtracting the linear function $\alpha t + \beta$ from $h_0^{\ell m}$ so as to define an approximation to the $(t \geq -\infty)$-integrated metric waveform, say $h_{\ell m}^{\rm old}(t) \equiv h_0^{\ell m}(t) - h_0^{\rm lin-fit}(t)$.

Here we will use a "new" (three-step) procedure, which starts with the same step (i), but modifies both steps (ii) and (iii) so as to get a better approximation to the exact metric waveform. First of all, we define an "adiabatic-like" approximation to the metric waveform,

$$\tilde{h}_{\ell m}(t) \equiv -\frac{\psi_4^{\ell m}(t)}{\omega_{\ell m}^2(t)} \tag{A4}$$

and use this to define

$$\tilde{h}_0^{\ell m}(t) \equiv h_0^{\ell m}(t) - \tilde{h}_{\ell m}(t). \tag{A5}$$

As $\tilde{h}^{\ell m}(t)$ is approximately equal to $h^{\ell m}(t)$ (because of the approximately adiabatic nature of the inspiral), we see from Eq. (A3) that $\tilde{h}_0^{\ell m}(t) = h_{\ell m}(t) - \tilde{h}_{\ell m}(t) + \alpha_{\rm exact} t + \beta_{\rm exact}$ will be closer to the unknown linear function $\alpha_{\rm exact} t + \beta_{\rm exact}$ than $h_0^{\ell m}(t)$ was. Therefore, the next step is to perform the linear fit on this $\tilde{h}_0^{\ell m}$ rather than on $h_0^{\ell m}(t)$ itself. Then, the last step (iii) consists, as in the past, in subtracting the resulting improved linear fit $\alpha t + \beta$ from the $(t \geq 0)$–integrated metric waveform $h_0^{\ell m}(t)$.

In addition, let us note that we perform the fit not on the whole time interval, but rather on a restricted time interval that cuts away the first cycles of the waveform. Finally, after doing several tests, we realized that the entire procedure leads to a physically more reliable metric waveform (see below) if $\tilde{h}_0^{\ell m}(t)$ is fitted not to a simple linear function, but rather to a quadratic[17] one, $h_0^{\rm quad-fit}(t) = \gamma t^2 + \alpha t + \beta$.

[16] Simple estimates based on the scaling $\kappa_2^T \propto R^5$ suggest that one needs to know $\Delta^{\rm tidal}\phi(\omega)$ with a fractional accuracy better than 20% to constrain NS radii to a relative precision of $\delta R/R \approx 4\%$. See also Ref. [22] for the prospects from a BH-NS system.

[17] We think that such a quadratic fit is needed for absorbing several effects that "pollute" the waveform, notably finite-extraction-

As emphasized in Ref. [46], we accept the integrated waveform if and only if its modulus exhibits a monotonic growth in time during the inspiral, consistently with the expected circularly polarized behavior of the metric waveform (as well as the curvature one)[18]. Figure 2 displays the metric waveforms (both for the `M2.9C.12` (left) and the `M3.2C.14` (right) models) obtained using this improved procedure. The time intervals where we fit the waveforms to get $h_0^{\rm quad-fit}(t)$ start respectively at $t_1/M = 294$ (model `M2.9C.12`) and at $t_1/M = 677$ (model `M3.2C.14`). Note how the modulus of both models exhibits a smooth monotonic behavior in time.

Appendix B: Cleaning the GW phase and Q_ω curves

We next provide more detailed information about the cleaning procedure of the NR GW phase advocated in Sec. IV and used to drive NR/AR comparisons. As we said in the main text, the final goal is to fit away the high-frequencies oscillations in the GW phase ϕ so as to get a clean and smooth Q_ω curve, Eq. (24). We recall that the idea is to fit $\phi(t)$ with an analytic expression that is modeled on the PN expansion. Defining the quantity

$$x(t,\phi_c) = \left\{\frac{\nu}{5}(t_c - t)\right\}^{-1/8}, \tag{B1}$$

one then fits the NR phase with an expression of the form

$$\phi = -\frac{2}{\nu}x^{-5}\left(1 + p_2 x^2 + p_3 x^3 + p_4 x^4 + \dots\right) + \phi_0, \tag{B2}$$

where t_c, ϕ_0, and the p_i's are free coefficients to be determined by the fit. Note that t_c can be thought of as defining a formal "coalescence" time. There are two delicate (correlated) points: (i) how many powers of x [possibly including also $x^n \ln(x)$ terms] one has to include in Eq. (B2), and (ii) on which (time) interval $I_t/M = (t_1, t_2)$ the approximate description of ϕ given by Eq. (B2) (and consequently of Q_ω) is reliable. The procedure to select the "best" time interval and to consistently assess the quality of our cleaned curves can be summarized as follows:

1. The initial time t_1 is chosen so as to eliminate as much as possible the most noisy part of the curvature frequency. In practical terms, this meant cutting at $t_1 = 1200$ for `M2.9C.12` data and $t_1 = 1000$ for `M3.2C.14` data. This is illustrated in the top-left panels of Fig. 16 (for `M2.9C.12` data) and of Fig. 17 (for `M3.2C.14` data), which show the curvature (dashed line) and metric (solid line) instantaneous GW frequency ω. In both plots, the first vertical line identifies the location of t_1.

2. For a given order of the polynomial, we found the right end, t_2, of the time window essentially, by trial and error, monitoring the behavior of several quantities. In particular, (i) we checked that the cleaned ω visually "averages" the raw ω, for both ψ_4^{22} and h_{22} data. This is illustrated in the top-right and bottom-right panels of Figs. 16-17, the raw data appearing as dashed lines, the cleaned data as solid lines. Then, (ii), we require that the phase difference $\phi^{\rm Clean} - \phi^{\rm Raw}$ averages to zero, which indicates that we have subtracted all the "secular" trends by means of our polynomial fit. The quantity $\Delta\phi^{\rm CleanRaw} = \phi^{\rm Clean} - \phi^{\rm Raw}$ (both curvature and metric) is displayed in the bottom-left panel of Figs. 16-17. The fact that it averages to zero is the indication that our fit caught the "secular" behavior of the phase, averaging away both (numerical) low-frequency and high-frequency oscillations.

3. For a fixed time window, the inspection of $\Delta\phi^{\rm CleanRaw}$ is also crucial for choosing the order of the polynomial in x, which we set to be of fourth-order. A 3rd-order one is clearly not enough to get the right trend of the frequency (and thus of Q_ω) up to the end of our preferred interval.

4. To better select the end t_2 of the time window, we found it useful to monitor the difference between the curvature and metric Q_ω's, namely $\Delta Q_\omega^{\rm c-m} = Q_\omega^{\rm curvature} - Q_\omega^{\rm metric}$. We typically choose the value of t_R in such a way that $\Delta Q_\omega^{\rm c-m}$ is always smaller than 0.2 on the frequency interval corresponding to I_t/M. This value can be estimated by comparing curvature and metric Q_ω's within the EOB. For example, for the NNLO model with $\bar{\alpha}_2 = 100$ one checks that $\Delta Q_\omega^{\rm c-m} \lesssim 0.2$ when $\omega \in [0.035, 0.055]$ for $\mathcal{C} = 0.12$, and $\Delta Q_\omega^{\rm c-m} \lesssim 0.2$ when $\omega \in [0.035, 0.063]$ for $\mathcal{C} = 0.14$. This gives us an idea of the level of $\Delta Q_\omega^{\rm c-m}$ that we can accept from our cleaned NR curves, so that we can choose the fitting time window accordingly.

In conclusion, to obtain the central NR-cleaned Q_ω curves labelled $\mathrm{IF_{HR}}500$ used in the core of the paper, we fixed $t_R/M = 3366$ for the `M2.9C.12` phase and $t_R/M = 2290$ for the `M3.2C.14` one. The time intervals (and the corresponding frequency ones) used to clean the other NR phases are also listed in Table III.

radius effects, remnant junk radiation, etc. In this respect, we also mention that Ref. [45], in the context of non-spherical star oscillations, found that a quadratic polynomial used in the recovery of h_{20} from ψ_4^{20} was a necessary choice to find a good agreement both with Abrahams-Price metric extraction and perturbative waveforms.

[18] Note however that small-amplitude, high frequency "ripples" are still present in the modulus. Their origin is however essentially numerical, as they are also present in the modulus of ψ_4^{22}.

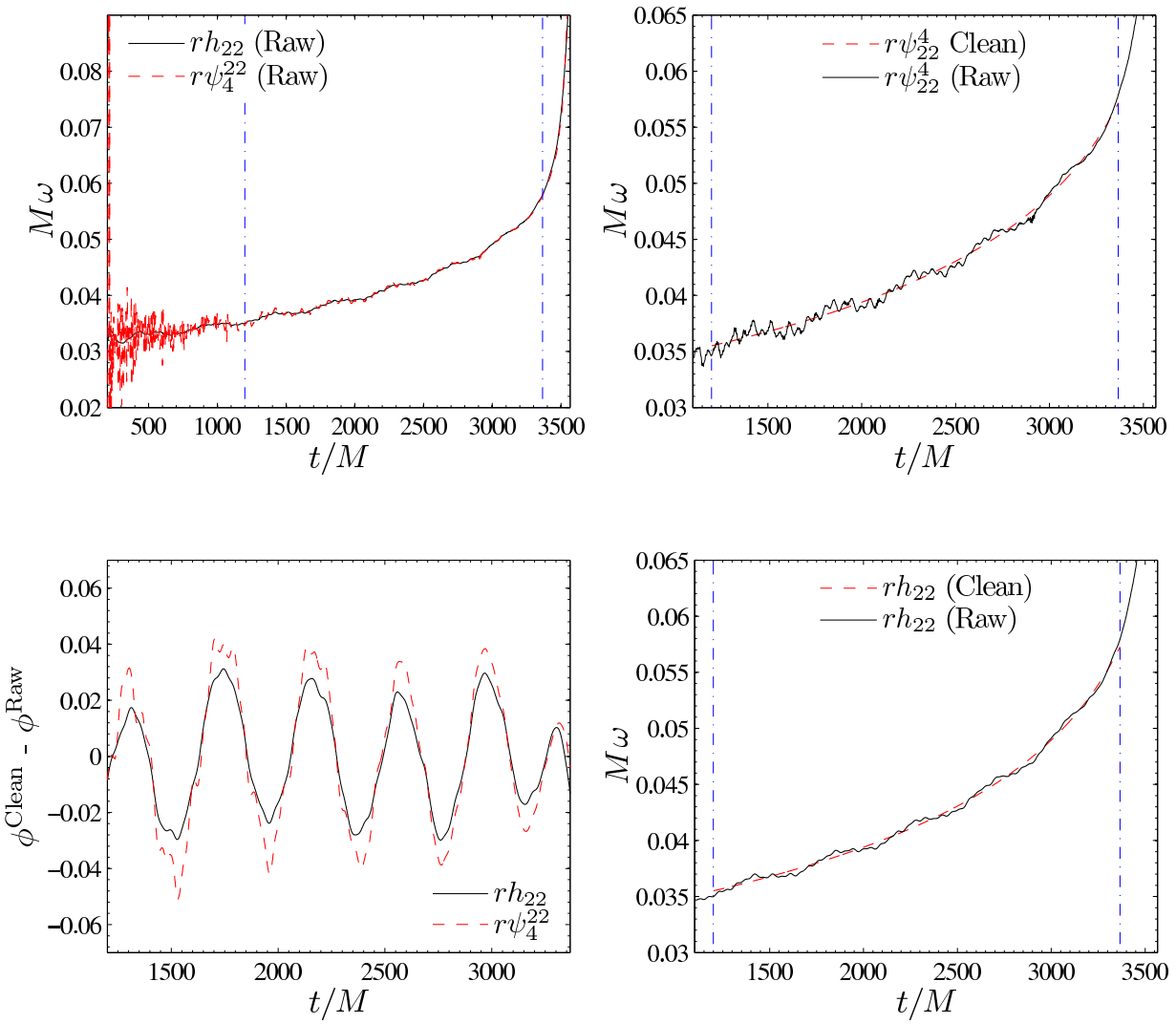

FIG. 16. Testing the fit of the GW phase of the `M2.9C.12` simulation. The top-left panel shows the time evolution of the frequency, computed from the metric and curvature waveforms. The bottom-left panel shows the deviation of the cleaned phase evolution with respect to the raw data; note that they average to zero. The right panels show the comparison of the frequency evolution of the cleaned and raw waveforms, for the curvature (top) and metric (bottom) waveforms.

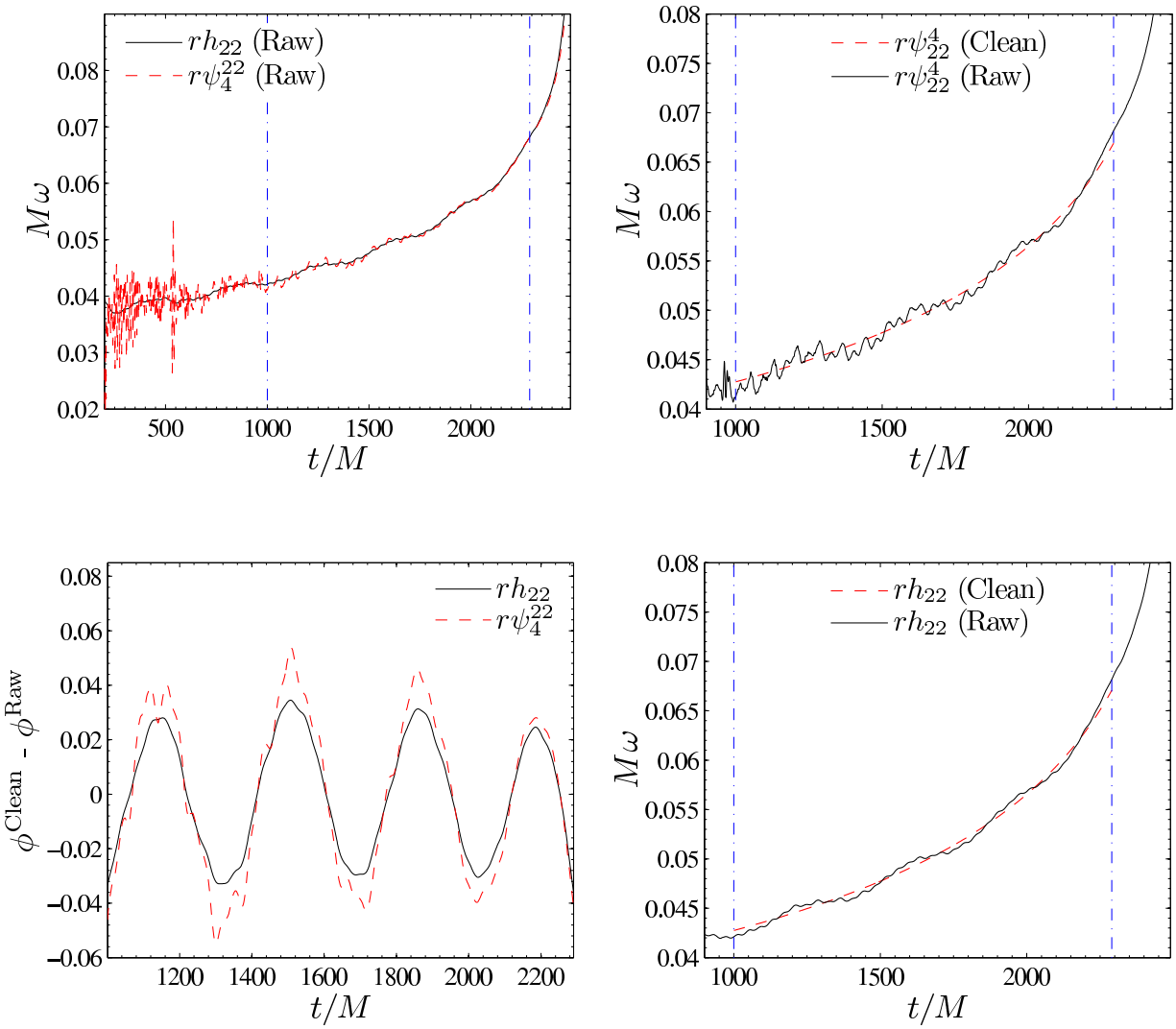

FIG. 17. The same as Fig. 16 but for the `M3.2C.14` simulation.

[1] L. Baiotti, T. Damour, B. Giacomazzo, A. Nagar, and L. Rezzolla, Phys. Rev. Lett. **105**, 261101 (2010), arXiv:1009.0521 [gr-qc].

[2] L. Baiotti, B. Giacomazzo, and L. Rezzolla, Phys. Rev. D **78**, 084033 (2008), arXiv:0804.0594 [gr-qc].

[3] M. Shibata and K. Uryū, Phys. Rev. D **61**, 064001 (2000), gr-qc/9911058.

[4] M. Anderson, E. W. Hirschmann, L. Lehner, S. L. Liebling, P. M. Motl, D. Neilsen, C. Palenzuela, and J. E. Tohline, Phys. Rev. D **77**, 024006 (2008), arXiv:0708.2720.

[5] T. Yamamoto, M. Shibata, and K. Taniguchi, Phys. Rev. D **78**, 064054 (2008), 0806.4007.

[6] L. Baiotti, B. Giacomazzo, and L. Rezzolla, Class. Quantum Grav. **26**, 114005 (2009), arXiv:0901.4955 [gr-qc].

[7] J. S. Read, C. Markakis, M. Shibata, K. Uryu, J. D. E. Creighton, and J. L. Friedman, Phys. Rev. D **79**, 124033 (2009).

[8] K. Kiuchi, Y. Sekiguchi, M. Shibata, and K. Taniguchi, Phys. Rev. D **80**, 064037 (2009), arXiv:0904.4551.

[9] K. Kiuchi, Y. Sekiguchi, M. Shibata, and K. Taniguchi, Phys. Rev. Lett. **104**, 141101 (2010).

[10] M. Anderson, E. W. Hirschmann, L. Lehner, S. L. Liebling, P. M. Motl, D. Neilsen, C. Palenzuela, and J. E. Tohline, Phys. Rev. Lett. **100**, 191101 (2008), 0801.4387.

[11] Y. T. Liu, S. L. Shapiro, Z. B. Etienne, and K. Taniguchi, Phys. Rev. D **78**, 024012 (2008), arXiv:0803.4193 [astro-ph].

[12] B. Giacomazzo, L. Rezzolla, and L. Baiotti, Mon. Not. R. Astron. Soc. **399**, L164 (2009).

[13] B. Giacomazzo, L. Rezzolla, and L. Baiotti, Phys. Rev. D **83**, 044014 (2011).

[14] L. Rezzolla, B. Giacomazzo, L. Baiotti, J. Granot, C. Kouveliotou, and M. A. Aloy, Astrophys. Journ. Lett. **732**, L6 (2011), arXiv:1101.4298 [gr-qc].

[15] L. Rezzolla, L. Baiotti, B. Giacomazzo, D. Link, and J. A. Font, Class. Quantum Grav. **27**, 114105 (2010), arXiv:1001.3074 [gr-qc].

[16] É. É. Flanagan and T. Hinderer, Phys. Rev. D **77**, 021502 (2008), arXiv:0709.1915.

[17] T. Hinderer, Astrophysical Journal **677**, 1216 (2008), arXiv:0711.2420.

[18] T. Damour and A. Nagar, Phys. Rev. D **80**, 084035 (2009), arXiv:0906.0096 [gr-qc].

[19] T. Binnington and E. Poisson, Phys. Rev. D **80**, 084018 (2009), arXiv:0906.1366 [gr-qc].

[20] T. Hinderer, B. D. Lackey, R. N. Lang, and J. S. Read, Phys. Rev. D **81**, 123016 (2010), arXiv:0911.3535 [astro-ph.HE].

[21] T. Damour and A. Nagar, Phys. Rev. D **81**, 084016 (2010), arXiv:0911.5041 [gr-qc].

[22] F. Pannarale, L. Rezzolla, F. Ohme, and J. S. Read, arXiv:1103.3526 (2011).

[23] K. Uryu, F. Limousin, J. L. Friedman, E. Gourgoulhon, and M. Shibata, Phys. Rev. D **80**, 124004 (2009), arXiv:0908.0579 [gr-qc].

[24] A. Buonanno and T. Damour, Phys. Rev. D **59**, 084006 (1999), arXiv:gr-qc/9811091.

[25] A. Buonanno and T. Damour, Phys. Rev. D **62**, 064015 (2000), gr-qc/0001013.

[26] T. Damour, Phys. Rev. D **64**, 124013 (2001), gr-qc/0103018.

[27] T. Damour and A. Nagar, Phys. Rev. D **79**, 081503 (2009), arXiv:0902.0136 [gr-qc].

[28] A. Buonanno *et al.*, Phys. Rev. D **79**, 124028 (2009), arXiv:0902.0790 [gr-qc].

[29] J. Vines, T. Hinderer, and É. É. Flanagan, arXiv:1101.1673 (2011), arXiv:1101.1673 [gr-qc].

[30] L. Blanchet and T. Damour, Phys. Rev. D **46**, 4304 (1992).

[31] T. Damour and A. Nagar, Phys. Rev. D **77**, 024043 (2008), arXiv:0711.2628 [gr-qc].

[32] T. Goodale, G. Allen, G. Lanfermann, J. Massó, T. Radke, E. Seidel, and J. Shalf, in *Vector and Parallel Processing – VECPAR'2002, 5th International Conference, Lecture Notes in Computer Science* (Springer, Berlin, 2003).

[33] E. Schnetter, S. H. Hawley, and I. Hawke, Class. Quantum Grav. **21**, 1465 (2004).

[34] D. Pollney, C. Reisswig, L. Rezzolla, B. Szilágyi, M. Ansorg, B. Deris, P. Diener, E. N. Dorband, M. Koppitz, A. Nagar, and E. Schnetter, Phys. Rev. D **76**, 124002 (2007).

[35] L. Baiotti, I. Hawke, P. Montero, and L. Rezzolla, in *Computational Astrophysics in Italy: Methods and Tools*, Vol. 1, edited by R. Capuzzo-Dolcetta (MSAIt, Trieste, 2003) p. 210.

[36] L. Baiotti, I. Hawke, P. J. Montero, F. Löffler, L. Rezzolla, N. Stergioulas, J. A. Font, and E. Seidel, Phys. Rev. D **71**, 024035 (2005).

[37] F. Banyuls, J. A. Font, J. M. Ibáñez, J. M. Martí, and J. A. Miralles, Astrophys. J. **476**, 221 (1997).

[38] E. Gourgoulhon, P. Grandclément, K. Taniguchi, J. A. Marck, and S. Bonazzola, Phys. Rev. D **63**, 064029 (2001).

[39] .

[40] R. H. Price and S. Rosswog, Science **312**, 719 (2006).

[41] M. Obergaulinger, M. A. Aloy, and E. Müller, Astronomy and Astrophysics **515**, A30 (2010).

[42] A. Nagar and L. Rezzolla, Class. Quantum Grav. **22**, R167 (2005), erratum-ibid. **23**, 4297, (2006).

[43] A. Nagar and L. Rezzolla, Class. Quantum Grav. **23**, 4297 (2006).

[44] J. N. Goldberg, A. J. MacFarlane, E. T. Newman, F. Rohrlich, and E. C. G. Sudarshan, J. Math. Phys. **8**, 2155 (1967).

[45] L. Baiotti, S. Bernuzzi, G. Corvino, R. De Pietri, and A. Nagar, Phys. Rev. D **79**, 024002 (2009), arXiv:0808.4002 [gr-qc].

[46] T. Damour, A. Nagar, M. Hannam, S. Husa, and B. Bruegmann, Phys. Rev. D **78**, 044039 (2008), arXiv:0803.3162 [gr-qc].

[47] T. Damour and A. Nagar, arXiv:0906.1769 (2009), arXiv:0906.1769 [gr-qc].

[48] J. Vines, E. E. Flanagan, and T. Hinderer, Phys.Rev. **D83**, 084051 (2011), arXiv:1101.1673 [gr-qc].

[49] T. Damour, B. R. Iyer, and A. Nagar, Phys. Rev. D **79**, 064004 (2009), arXiv:0811.2069 [gr-qc].

[50] R. Fujita and B. R. Iyer, Phys.Rev. **D82**, 044051 (2010), arXiv:1005.2266 [gr-qc].

[51] L. Blanchet and T. Damour, Annales Poincare Phys.Theor. **50**, 377 (1989).
[52] L. Blanchet, Phys.Rev. **D51**, 2559 (1995), arXiv:gr-qc/9501030 [gr-qc].
[53] T. Damour and A. Nagar, Phys. Rev. D **76**, 064028 (2007), arXiv:0705.2519.
[54] M. Boyle *et al.*, Phys. Rev. D **78**, 104020 (2008), arXiv:0804.4184 [gr-qc].
[55] T. Damour, A. Nagar, and M. Trias, (2011), in preparation.
[56] S. Bernuzzi and A. Nagar, Phys. Rev. D **81**, 084056 (2010).
[57] T. Damour, B. R. Iyer, and B. S. Sathyaprakash, Phys. Rev. D **62**, 084036 (2000), arXiv:gr-qc/0001023.
[58] L. Blanchet, Living Rev. Relativ. **9**, 4 (2006).
[59] T. Damour, A. Nagar, E. N. Dorband, D. Pollney, and L. Rezzolla, Phys. Rev. D **77**, 084017 (2008), arXiv:0712.3003 [gr-qc].
[60] D. Pollney, C. Reisswig, E. Schnetter, N. Dorband, and P. Diener, "High accuracy binary black hole simulations with an extended wave zone," (2009), arXiv:0910.3803 [gr-qc].
[61] M. Hannam, S. Husa, B. Bruegmann, and A. Gopakumar, Phys. Rev. D **78**, 104007 (2008), arXiv:0712.3787 [gr-qc].
[62] T. Damour and O. M. Lecian, Phys. Rev. D **80**, 044017 (2009), arXiv:0906.3003 [gr-qc].